A novel approach to identifying mantle-equilibrated zircon by using trace element chemistry

Ziqin Ni[1], Ricardo Arevalo Jr.[1], Philip Piccoli[1], Barry Reno[2]

[1]University of Maryland, College Park, MD, 21401

[2]Northern Territory Geological Survey, Darwin, NT, 0800

Corresponding author: Ziqin Ni (zni@umd.edu)

Key Points:

- Zircon Ce/Ce* oxybarometry
- Ti-in-zircon thermometry
- Mantle oxygen fugacity

Abstract

One of the requirements for inferring local mantle redox states via zircon Ce/Ce* oxybarometry and Ti-in-zircon thermometry is to select mantle-equilibrated zircon (i.e., unaltered magmatic zircon without interaction to hydrosphere). Traditional protocols for identifying mantle-equilibrated zircon require comprehensive examination of whole rock geochemistry in addition to zircon morphology, texture, and trace element and isotopic measurements to obtain information for zircon saturation context, source melt petrogenesis, and post-magmatic history. This study proposes a simple filter scheme for selecting mantle-equilibrated zircon using trace element systematics alone (P, Ti, Y, Nb, REE, Hf, Th, U). A total of 13 filtering criteria are synthesized from previous studies based on simulations, experiments, and compiled global datasets, all of which help to provide geological context and ultimately constrain the inferred melt redox state from three perspectives: (1) mineral inclusions; (2) source melt petrogenesis; and, (3) zircon saturation context. The filter scheme presented here, which is based on detailed classifications of zircon morphology/texture and host rock compositions of 2317 zircon analyses from 30 independent references, is shown to distinguish non-magmatic zircon (Group III), magmatic zircon with significant inclusions and/or sourced from highly enriched source melt (Group II), and mantle-equilibrated zircon (Group I). A case study of Group I mantle-equilibrated zircon from Greenland suggests that their respective mantle source has reached ΔFMQ -0.5 since ca. 2950 Ma. Future applications of this filter scheme include studies of out-of-context detrital and/or xenocrystic zircon.

Plain Language Summary

Zircon is a robust accessory mineral commonly found in many rock types. The Ce/Ce* and Ti content in zircon provide valuable insights about the redox states of local magmatic environment from which it crystallized. When it comes to study of mantle redox state via zircon Ce/Ce* oxybarometry and Ti-in-zircon thermometry, one of the requirements is to select mantle-equilibrated zircon (i.e., unaltered magmatic zircon without interaction to hydrosphere). Traditionally, such selection relies on comprehensive examinations of zircon and their host rock (i.e., whole rock geochemistry, zircon morphology, texture, and trace element and isotopic measurements) in order to obtain information for zircon saturation context, source melt petrogenesis, and post-magmatic history. This study, however, presents a simple filter scheme that facilitates the selections of mantle-equilibrated zircon and provides quick insights about zircon petrogenesis using trace element systematics alone (P, Ti, Y, Nb, REE, Hf, Th, U).

1. Introduction

Zircon ($ZrSiO_4$) is a robust accessory mineral commonly found in many rock types, capable of surviving multiple igneous or metamorphic events, weathering and transport, hydrothermal alteration, etc. In the zircon crystal lattice, $^{VIII}Zr^{4+}$ may be exchanged for a range of incompatible trace elements, such as large ion lithophile elements (LILE; e.g., U and Th) and high field strength elements (HFSE; e.g., Hf and rare earth elements, REE). Due to low modal abundances, the fractionation of zircon has a little effect on the bulk melt composition (major oxides, e.g., SiO_2) and magmatic environment (e.g., oxygen fugacity, temperature). Consequently, zircon trace element and isotope systematics can provide valuable insights about the local magmatic environment from which it crystallized. For example, studies of zircon chemistry have been used to infer: melt crystallization temperatures based on Ti concentrations in zircon (e.g., Watson and Harrison, 2005; Ferry and Watson, 2007; Fu et al., 2008; Siégel et al., 2018); the timing of crystallization and/or metamorphism from U-Th-Pb radiometric dating (e.g., Zheng et al., 2004; Tichomirowa et al., 2013); the provenance of source material from concentrations of LILEs and HFSEs (e.g., Hoskin and Ireland, 2000; Belousova et al., 2002; Grimes et al., 2007, 2015; Chapman et al., 2016); and, the degree of crustal assimilation in magmatic systems based on coupled O-Hf isotopes (e.g., Hawkesworth and Kemp, 2006; Trail et al., 2007; Page et al., 2007; Cavosie et al, 2009; Spencer et al., 2017).

Of particular importance, magmatic oxygen fugacity (or fO_2) has been inferred from the abundances of multivalent elements, namely Ce (3+, 4+) and Eu (2+, 3+), relative to other monovalent REE (3+ only). In zircon, REE^{3+} can replace Zr^{4+} in a coupled substitution with additional cations (e.g., P^{5+}) to balance charge. The compatibilities of trivalent REE in zircon increase systematically from La to Lu due to progressively smaller ionic radii with increasing atomic number (commonly termed the lanthanide contraction; Figure 1). However, under oxidizing conditions, a greater proportion of Ce is present as the higher Ce^{4+} valence state, resulting in preferential incorporation into the zircon structure (relative to Ce^{3+}) due to its smaller ionic size and equivalent charge to Zr^{4+}. This substitution bias results in a "positive spike" of Ce relative to nearby trivalent elements La and Pr in normalized composition diagrams, enabling the quantification of a Ce anomaly as: $Ce/Ce^* = Ce_N/\sqrt{La_N \times Pr_N}$. In comparison, under reducing conditions, a greater proportion of Eu takes on the lower Eu^{2+} valence state. Because Eu^{2+} is too large to fit into the zircon structure without incurring significant lattice strain, Eu exhibits a "negative trough" relative to neighboring trivalent Sm and Gd, defining a Eu anomaly as: $Eu/Eu^* = Eu_N/\sqrt{Sm_N \times Gd_N}$.

Magmatic fO_2, as recorded by accessory zircon, is an important control on elemental behavior, such as solubility (e.g., soluble Fe^{2+} versus insoluble Fe^{3+}), mobility (e.g., mobile UO_4^+ versus immobile U^{4+}), chemical affinity (e.g., siderophile S at low fO_2 versus lithophile S at high fO_2), and compatibility (e.g., compatible Eu^{2+} versus incompatible Eu^{3+} in plagioclase). Understanding the oxygen fugacity of the upper mantle in the early Earth is particularly valuable for quantitatively describing processes associated with planetary differentiation (e.g., Frost et al., 2008; Frost and McCammon, 2008; Yang et al., 2014) and the evolution of atmospheric composition (e.g., Kump et al., 2001, Trail et al., 2011; Lee et al., 2014). Consequently, Ce/Ce* (and to a lesser extent Eu/Eu*) preserved in zircon may provide powerful insights into the composition and dynamics of the Earth's deep interior and surface in the geological past.

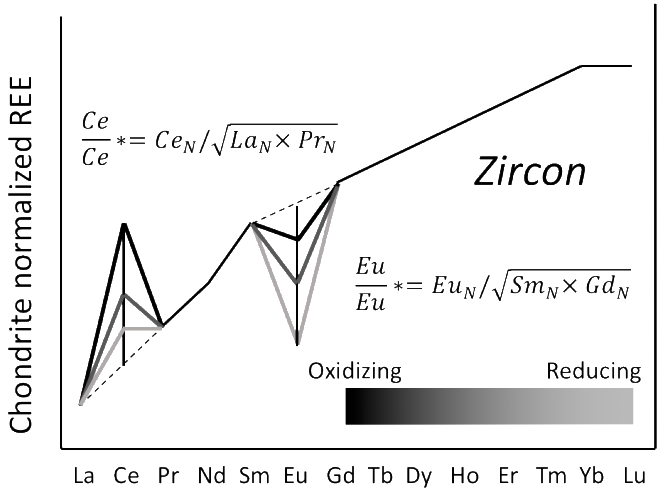

Figure 1. Schematic chondrite normalized pattern of REE in zircon. Ce/Ce* and Eu/Eu* are calculated as $Ce_N/\sqrt{La_N \times Pr_N}$ and $Eu_N/\sqrt{Sm_N \times Gd_N}$ respectively, where the subscript N indicates trace element values normalized to CI chondrites (McDonough and Sun, 1995). As the oxygen fugacity of the system increases (darker shade of gray), Ce/Ce* is expected to increase whereas Eu/Eu* is expected to decrease. The majority of terrestrial magmatic zircon will have both positive Ce/Ce* and negative Eu/Eu*.

1.1 Quantitative zircon Ce/Ce* oxybarometry and Ti-in-zircon thermometry

Experimental studies demonstrate a variety of empirical relationships between fO_2 in silicate melts and Ce/Ce* recorded in zircon (Trail et al., 2011 & 2012; Burnham and Berry, 2012; Smythe and Brenan, 2015 & 2016). In general, such relationships are most sensitive to the alumina and water concentration of the melt, and to a lesser degree the temperature of the melt when the system reaches zircon saturation. As such, experimentally-calibrated Ce/Ce* oxybarometry and Ti-in-zircon thermometry are often applied together to provide a streamlined estimation of melt redox state, which are often reported as orders of magnitude deviations from the fO_2 of mineral assemblage fayalite-magnetite-quartz (FMQ) at a specific temperature, i.e., ΔFMQ (Chou, 1978).

Multiple studies have attempted to constrain zircon Ce/Ce* in different environments, such as anhydrous peralkaline melts at high temperature (i.e., 1300 ℃; Burnham and Berry, 2012). However, such conditions are less likely to precipitate appreciable amount of zircon due to high zircon solubilities but low Zr availability in mafic magmas (Watson and Harrison, 1983; Boehnke et al., 2013; Shao et al., 2019). Statistically, the majority of natural zircon crystallizes in hydrous alumina-saturated melts (i.e., determined by the molar ratio of $Al_2O_3/(Na_2O + K_2O)$, or A/NK > 1) at relatively lower temperatures (e.g., ~800 ℃). Therefore, the empirical relationship that most universally describes Ce partitioning behavior in natural zircon is from Trail et al. (2012),

$$\ln\left(\frac{Ce}{Ce^*}\right)_{CHUR} = (0.1156 \pm 0.0050) \times ln(fO_2) + \frac{13860 \pm 708}{T(K)} - (6.125 \pm 0.484) \quad \text{Eqn (1),}$$

where the experiments were conducted at 10 kbar and 800 – 1300 ℃ with 2 to 10 wt% H_2O (Trail et al., 2012).

The zircon crystallization temperature T in Eqn (1) can be inferred from the Ti concentration in zircon following the quantitative relationship below (Ferry and Watson, 2007):

$$log(\,Ti\ in\ zircon\ ppm) = (5.711 \pm 0.072) - \frac{4800 \pm 86}{T(K)} - \log(a_{SiO_2}) + log(a_{TiO_2}) \qquad \text{Eqn (2).}$$

The activity of SiO_2 (a_{SiO_2}) and TiO_2 (a_{TiO_2}) are dimensionless quantity that describes the chemical potential of SiO_2 and TiO_2 of the system relative to quartz and rutile, respectively. In the literature, the value of a_{SiO_2} is commonly assumed to be unity as zircon most commonly crystallizes from melt that is close to quartz saturation (Ferry and Watson, 2007). The value of a_{TiO_2} in silicic melts at appropriate magmatic temperature is typically between 0.6 and 1, and it can be estimated based on the crystallization of mineral phases at equilibrium with zircon, such as rutile (a_{TiO_2}=1), and ilmenite and/or titanite (a_{TiO_2}= 0.6) (Watson et al, 2006; Ferry and Watson, 2007). In applications to quartz-free crustal rocks and/or detrital zircon with limited or no geological context, the uncertainty in a_{SiO_2} and a_{TiO_2} will impose only limited effects on calculated temperatures. For example, assuming $a_{SiO_2} = 1$ and $a_{TiO_2} = 1$ yields an uncertainty of up to 70 ℃ uncertainty in calculated temperature (Ferry and Watson, 2007).

1.2 Advantages and limitations of zircon geochemical proxies

The greatest promise of coupled Ce/Ce* oxybarometry and Ti-in-zircon thermometry is the streamlined estimation of melt redox state; theoretically, any zircon crystal of magmatic origin (even out-of-context detrital and xenocrystic samples) can provide an independent evaluation of melt dynamics, requiring only a limited set of chemical measurements. However, the direct application of these methods to magmatic zircon can generate an unrealistic spread in calculated melt redox states that extends below conditions expected at the core mantle boundary (ΔFMQ < -4; McCammon, 2005) to those found in the modern atmosphere (ΔFMQ > +10; McCammon, 2005). This wide range of inferred redox states recorded by zircon can be explained by: (1) melt contributions from multiple sources (mantle magmas, assimilated crustal rock, etc.); (2) dynamic growth conditions (disequilibrium crystallization, mineral decomposition during metamorphism, etc.); and/or (3) modification of zircon trace element concentration via post-magmatic processes (subsolidus crystallization, hydrothermal alteration, etc.). These dynamic geological processes can diversify the composition of source melt, and change trace element signatures in zircon syn- and/or post- zircon saturation. As a result, a zircon may be described by a characteristic confidence level that it has retained information about the mantle (including local redox state).

Historical applications of Ce/Ce* oxybarometry in zircon have focused on reporting melt redox states of mantle-equilibrated zircon as a way to constrain the inferred fO_2 variation observed in natural systems. Mantle-equilibrated zircon refer to unaltered magmatic zircon that crystallized from source melt without interaction with the hydrosphere and/or assimilation of exogenous materials (e.g., sediments, crustal materials). Evaluation of zircon mantle-equilibration state traditionally requires a number of analytical protocols including (but not limited to):

- determination of whole rock chemistry to estimate the source melt composition, calculate apparent zircon/melt partition coefficient for Ce, infer the crystallization behavior (equilibrium versus disequilibrium) and growth environment of zircon;
- petrographic examination and/or chemical mapping (e.g., via back-scattered electron (BSE) or cathodoluminescence (CL) imaging) to characterize zircon morphology and texture, identify

mineral or fluid inclusions, evaluate intragranular and intergranular chemical and isotopic variation based on zoning, and infer petrogenetic history (Corfu et al., 2003; reference therein);

- measurement of isotopes in individual zircon crystal. For example, U-Pb dating to understand the population of zircon saturation in host rock, and oxygen isotopes to screen zircon that crystallized from source melt with negligible interaction to hydrosphere, and within the mantle-equilibration zone ($\delta^{18}O$ 5.3 $\pm$ 0.3 ‰, 2sd) (Valley et al, 1998); and,
- chemical filtering to exclude zircon that carry trace element signatures indicative of mineral inclusions (e.g., apatite, etc.; Bell et al., 2019) and non-magmatic features (i.e., hydrothermal and metamorphic zircon; Hoskin & Black, 2002; Hoskin, 2005).

These requirements are often necessary to obtain a thorough understanding of zircon saturation conditions, constrain statistical variances, and add confidence to inferred melt redox states. For instance, the application of these methods has enabled the demonstration that mantle-equilibrated zircon center around the FMQ buffer (e.g., Trail et al., 2011). However, such strict protocols also reduce the size of viable data sets and ultimately undermine the capability/advantage of the method by requiring extensive analyses that may not be feasible given financial (cost), programmatic (time), and/or logistical (sample mass) limitations. For example, in situ measurements of oxygen isotope in zircon require Secondary Ion Mass Spectrometry (SIMS), which are not only expensive but also demand a critical mass of zircon for in situ analysis (Valley, 2003).

1.3 Purpose of this study

The purpose of this study is to establish a multidimensional filter scheme that facilitates the determination of mantle source oxygen fugacity from magmatic zircon based only on a narrow range of trace element systematics, without reducing the accuracy of inferred fO_2 estimates. Instead of relying on extensive contextual observations (e.g., petrography, whole rock compositions, and oxygen isotope ratios), trace element abundances and dynamics are used to isolate zircon that have experienced diverse geological processes (e.g., inclusions, subsolidus crystallization, crystallized from melt with potential interaction to hydrosphere etc.), so that the combined filters can screen effectively for mantle-equilibrated zircon (Figure 2). The selectivity of these chemical criteria is evaluated objectively by applying the methods developed here to robust, publicly available zircon databases. Zircon with the greatest compositional similarity to the canonical trace element chemistry of mantle-equilibrated zircon should theoretically have the highest probability of recording (and preserving the signature of) the local mantle redox state.

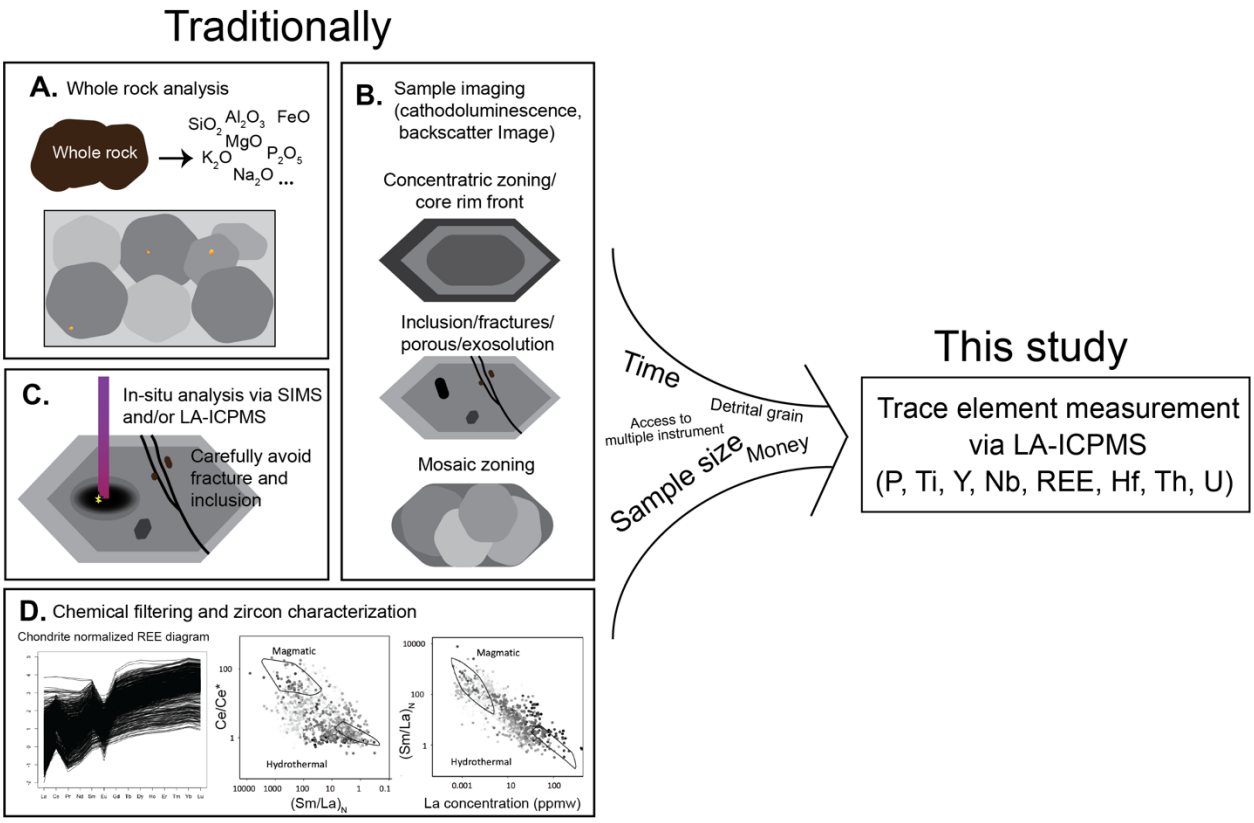

Figure 2. A comparison diagram between traditional approach and this study at screening mantle-equilibrated zircon.

2. Zircon data compilation and preparation

In order to evaluate the effectiveness of the filtering criteria proposed here, we compiled a zircon dataset that includes samples from a wide geographical and age distribution. The data were compiled from independent 30 references that measured the following trace element concentrations: P, Ti, Y, Nb, REE, Hf, Th, U (see Supplementary Material I and dataset references below). Zircon entries without trace element concentrations listed, or with values below detection limits, are not used in this study. The dataset used in this study contains data for 2173 individual zircon analyses.

To investigate the relationship between host rock and zircon trace element systematics, each zircon entry was labelled with silica content and A/NK values of their host rocks, and further classified based on the type of their host rock (i.e., igneous, metamorphic, detrital, carbonatite, kimberlite, and mineral deposits). The origin of each individual zircon was deduced from BSE and CL imaging (i.e., magmatic, magmatic with inclusion, magmatic with metamorphic rims, magmatic with hydrothermal rims, metamorphic, hydrothermal, metamict). The classification was left as blank if no host rock or contextual information was provided in the literature. Such detailed classification and labelling facilitate the validation of the trace element systematics summarized from simulations, experiments and measurements in the literature summarized in section 3, and further demonstrate the sensitivity of the proposed filtering scheme in sections 4 and 5.

The Ce/Ce*, Ti-in-zircon temperature, and melt redox state were calculated for all 2173 zircon entries compiled here using Eqn (1) and (2), assuming unity a_{SiO_2} and a_{TiO_2} respectively. By propagating errors associated with Ti-in-zircon temperature ($\pm$ 70 ℃; Ferry and Watson) and 5% (2sd) analytical uncertainty on REE measurement, the uncertainty for reported ΔFMQ value here is about $\pm$ 2 log units.

3. Trace element systematics of zircon

As mentioned in section 1.2, the variance of inferred melt redox state derived from Ce/Ce* in zircon can be attributed to three categories: (1) mineral inclusions; (2) source melt petrogenesis; and (3) saturation context of zircon. The trace element systematics of zircon associated with these processes have been explored independently in previous studies via simulations, experiments, and global datasets, which are summarized below as foundations for selecting filtering criteria.

3.1 Mineral inclusions in zircon

Mineral inclusions are common in igneous zircon. Some inclusions act as nucleation sites for crystallizing zircon crystals in melt (i.e., primary inclusion); others, however, are alteration or exsolution features reflecting post-magmatic processing (e.g., hydrothermal alteration, metamorphism, exsolution features) (i.e., secondary inclusion). The scale of such intragranular heterogeneity varies from visible micron-sized inclusions to nanoscale trace element enrichment zones (Corfu et al., 2003; Anderson et al., 2008; Hofmann et al., 2014; Bell et al., 2015). Therefore, sampling of inclusion phases and/or local enrichment zones cannot be completely avoided even with high-resolution petrographic imaging. Spatially resolved analytical techniques that characterize exceedingly small sample volumes (e.g., Secondary Ion Mass Spectrometry, SIMS) are particularly susceptible to disproportionate sampling of trace amounts of inclusions or nanoscale enrichments; the chemical signatures of localized features may be artificially amplified by individual spot analyses.

Based on this study, measurements of zircon plagued by primary and secondary inclusions can lead to up to 15 orders of magnitude variation in inferred melt redox states, as such phases may inflate estimated Ti-in-zircon temperatures (e.g., via excess Ti derived from titanite and magnetite) and/or attenuate the magnitude of observed Ce/Ce* anomalies (e.g., via overprinting REE signatures). Simple two-component mixing between a variety of phases commonly included in zircon (i.e., apatite, titanite, allanite, xenotime, and monazite) and the most primitive zircon grain from the case study reviewed in Section 5.2 (see below) demonstrates that as little as 0.0001 wt % of monazite and allanite inclusions will reduce Ce/Ce* by more than 80%. Interestingly, 0.5 wt % of inclusions enriched in light REE will overprint the Ce/Ce* signature completely (Figure 3).

Therefore, due to the high sensitivity of Ce/Ce* oxybarometry to mineral inclusions and the potential risks of sampling them, filtering magmatic zircon for such based on diagnostic chemical trademarks is one of the most important steps for constraining variation in inferred melt redox states.

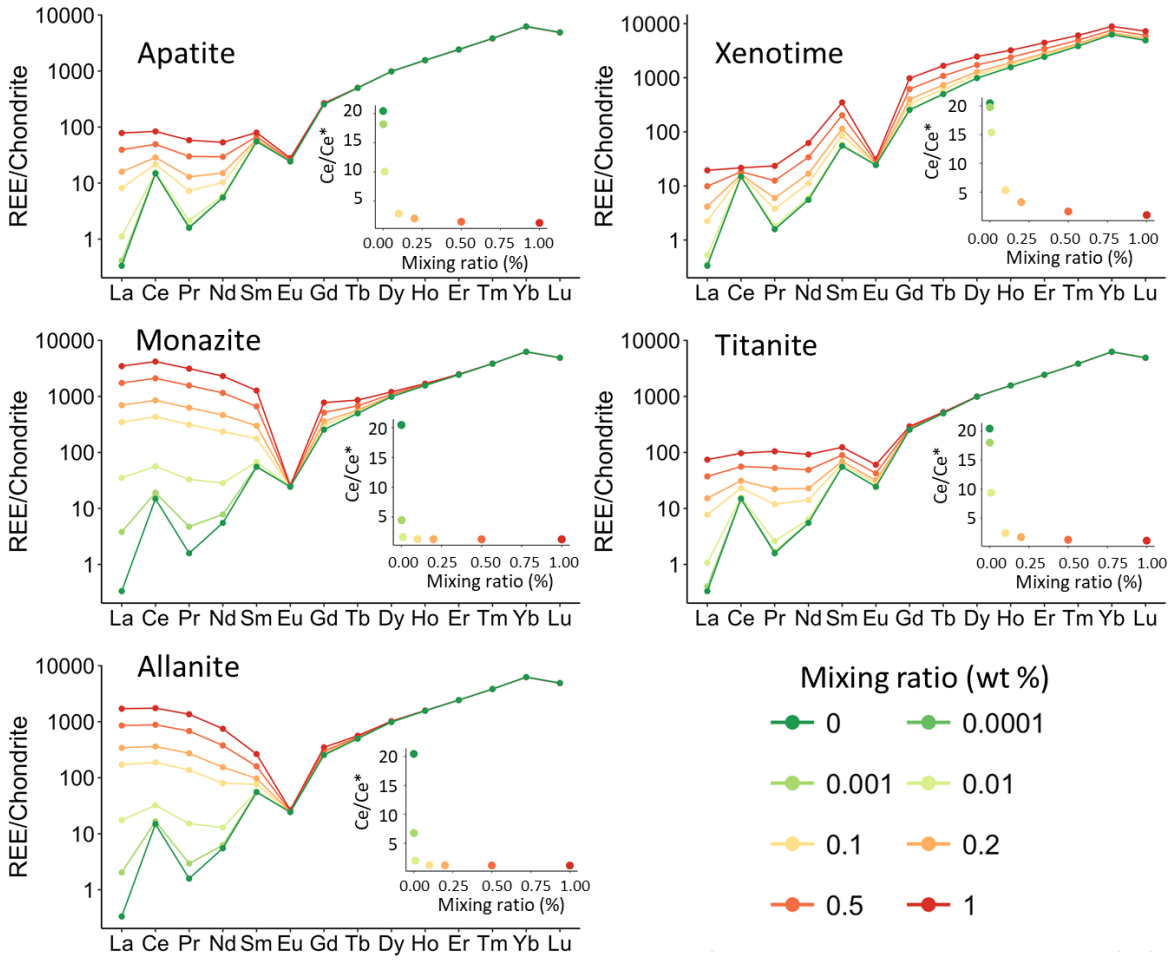

Figure 3. Mixing models between zircon and potential inclusions across a range of mixing proportions demonstrates the sensitivity of Ce/Ce* to chemical overprinting. The REE concentration of unadulterated zircon is modeled after sample 524994 Zircon 76, the most primitive zircon grain from the case study reviewed in Section 5.2. The average REE concentration of apatite is from Zhong et al. (2018a), and the compositions of the other phases (xenotime, monazite, titanite, allanite) are from Bea et al. (1996; see Supplementary Material II). The insets describe the relationship between Ce/Ce* and the mixing ratio of inclusions.

Historical criteria for filtering hydrothermal zircon include Ce/Ce*, La concentration, $(Sm/La)_N$, and light rare earth element index (LREE_I), calculated as the concentrations of Dy/Nd+Dy/Sm. Based on petrographically predetermined magmatic and hydrothermal zircon, filtering schemes previously proposed in literature targeting the selection unaltered magmatic zircon are Ce/Ce* $\leq$ 100, La between 0.002 to 0.5 ppm, $(Sm/La)_N$ between 30 to 1000, and LREE_I > 60 (Hoskins 2005; Bell et al., 2019). Because Ce/Ce* is one of the input parameters for calculating oxygen fugacity via Eqn (1), the range of Ce/Ce* is especially important for accurately determining melt redox state. The traditional upper boundary Ce/Ce* $\leq$ 100 is adopted as a filter for magmatic zircon because Ce/Ce* >100 is approximately equivalent to an unrealistic magmatic environment as oxidized as modern atmosphere (ΔFMQ > +10; McCammon, 2005). The lower boundary of Ce/Ce*, however, cannot be directly inferred because it varies with the amount of REE in the melt, as well as the mixing ratio of inclusions in the sample.

Therefore, instead of setting a lower boundary of Ce/Ce*, the other three parameters, La concentration, $(Sm/La)_N$, and LREE_I, are used to change the fraction of inclusions within zircon.

Figure 4 shows the sensitivity of La concentration, $(Sm/La)_N$, and LREE_I for filtering mineral inclusions of different mixing ratio to zircon. La < 0.1 ppm is the most sensitive parameter that is able to filter out zircon with mineral inclusions as low as 0.0001 wt%, but such sensitivity is reduced by up to three orders of magnitude if La < 0.5 ppm is used instead. Similarly, $(Sm/La)_N$ > 100 is able to discern 0.0001 wt% monazite and allanite, but relaxing the requirement to $(Sm/La)_N$ > 30 masks up to 0.2 wt% of xenotime, which can attenuate Ce/Ce* by 80 %. Although LREE_I is the least sensitive parameter among these three, it is important to use an additional La-independent criterion to monitor inclusions because the analytical uncertainties of La measurements in zircon may be high due to analytical limits of detection. Further, because trace element concentrations of each mineral inclusion vary over two orders of magnitudes in natural samples, multidimensional criteria can increase the filtering power and reduce the probability of detecting inclusions.

Therefore, the boundaries of current filtering scheme are updated to identify samples with the highest probabilities of reflecting unaltered mantle-equilibrated magmatic zircon: La concentration between 0.1 and 0.002 ppm, $(Sm/La)_N$ between 100 and 1000, and LREE_I > 60. In addition, Ce/Ce* $\leq$ 100 is adopted to distinguish magmatic zircon.

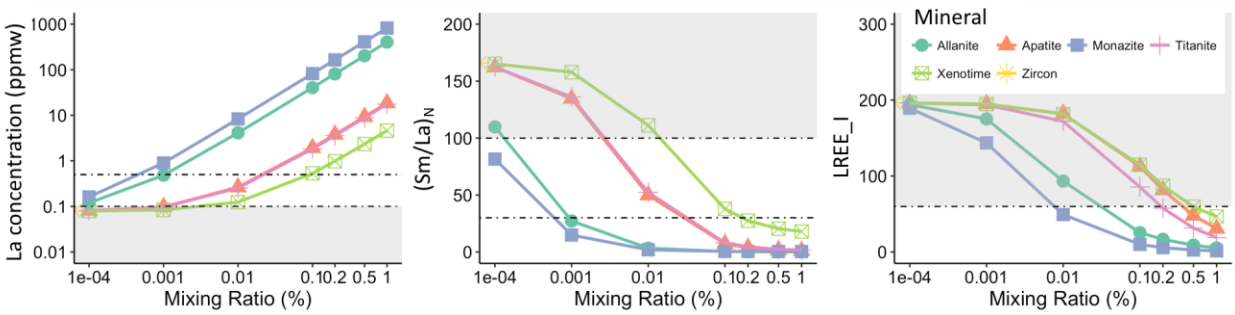

Figure 4. A sensitivity comparison between all three inclusion indicators: La concentration; $(Sm/La)_N$; and, LREE_I as a function of mixing ratio (%). The shaded areas represent regions that will be selected (or accepted) by the filter scheme.

3.2 Source melt petrogenesis

Zircon starts to crystallize when the Zr availability in the system (e.g., source melt) is greater than or equal to the zircon saturation content. Zircon saturation content, or the minimum Zr concentration required to precipitate zircon in the melt, tends to decrease with an increasing degrees of melt polymerization and/or decreasing magma temperature (Boehnke et al., 2013; Hanchar and Watson, 2003). For example, the zircon saturation content in basaltic magma is about 2000 to 30000 ppmw Zr (Shao et al., 2019) but reduces to ~100 ppmw in silicic magma (Watson, 1979). The availability of Zr in melt, however, is constrained and remains relatively constant; for example, the average Zr content in global mid ocean ridge basalt (e.g., ~100 ppmw; e.g., Arevalo and McDonough, 2010) is similar to the

composition of the bulk continental crust (~130 ppmw Zr; e.g., Rudnick, 1995). Despite similar Zr availability, the zircon saturation contents of these two systems are dramatically different because melt polymerization serves as a dominant control, and prevents the crystallization of zircon in mantle-derived magma unless the source melt interacts with metasomatic fluids or assimilates felsic materials (e.g., marine sediments, slab-derived melt, or crusts). In fact, the source melts of most zircon in ultramafic and/or mafic host rocks in compiled dataset are often interpreted as melt products of metasomatized mantle-wedge, or contaminated mantle-derived melt that mixed with slab-derived fluids or crustal materials during ascent (e.g., Janoušek et al 2019; Robinson et al., 2015; Tichomirowa et al., 2012; Sun et al., 2018; Vilalva et al., 2019, etc.). Because fluids and surface materials have undergone various low temperature processes (chemical and mechanical weather, erosion, etc.) and commonly possess enriched incompatible trace element abundances, assimilation of these materials can easily overprint the inherited fO_2 signatures from the original mantle source.

Historical studies of source melt petrogenesis focus on whole rock geochemistry and isotopic measurements of zircon crystals (e.g., Robinson et al., 2015; Liang et al, 2018; Janoušek et al., 2019). Specifically, whole rock geochemistry provides insights about the provenance and composition of the source melt, and oxygen and Hf isotopes of zircon track the interaction to metasomatic fluids and the contribution of felsic materials. In this study, instead of relying on whole rock or detailed isotopic analyses, previously developed trace element proxies are used to infer the formation and composition of source melt.

3.2.1 Source melts from igneous sources: P ≤ 750 ppm and (REE+Y)/P molar ratio > 1

Zircon is commonly found in granitic systems, but felsic melt can derive from both igneous sources (I-type granite, alumina-saturated metaluminous melt) and sedimentary sources (S-type granite, alumina-oversaturated peraluminous melt). Generation of melt from a sedimentary protolith implies little to nothing about mantle redox conditions, so zircon from S-type granitoids provide less insight into the deep Earth compared to mantle-equilibrated zircon.

Zircon P concentration provides a gauge to identify the type of granitic protolith. The average P concentration of global MORB is ~600 ppmw (Arevalo Jr. and McDonough, 2010). Due to its incompatibility to most major minerals, the P concentration of a melt may increase as the magma differentiates until apatite precipitates. Apatite ($Ca_5(PO_4)_3(OH, Cl, F)$) is a common accessory phase that crystallizes prior to zircon saturation in metaluminous melt (Lee et al., 2014), but dissolves in peraluminous melt as magmatic differentiation continues (Mysen et al., 1997). Despite the insignificant difference of bulk rock P_2O_5 concentration between S-type and I-type granites, the saturation and dissolution of apatite control the availability of P in residual melts.

In general, S-type zircon inherit a higher P concentration, whereas only 10 % of I-type zircon have P concentration > 750 ppm (Burnham and Berry, 2017). Moreover, coupled substitution between P^{5+} and $(REE,Y)^{3+}$ for Zr^{4+} becomes dominant in melt with a higher P concentration. S-type zircon are observed to have a strong linear correlation between the molar ratios for REE+Y and P, whereas I-type zircon are observed to have (REE +Y)/P molar ratio > 1. The lack of linear correlation in I-type zircon implies preference of additional REE incorporation mechanisms in P-deficient metaluminous melt. In a case study by Burnham and Berry (2017), the authors suggest that the combined criteria P ≤ 750 ppm and (REE+Y)/P molar ratio > 1 enables the isolation 96% of I-type zircon based on 144 zircon analyses from characterized S-type and I-type granites.

Similar source melt information has been inferred form Eu/Eu* (Wang et al., 2012, see section 3.3.4) and Al content in detrital zircon (Trail et al., 2017). Although they are not specifically addressed in these sections, they could be considered as alternative criteria for differentiating source of source melt.

3.2.2 Limited interaction with fluids and surface materials: U/Yb ≤ 20 and/or Th/Yb ≤ 10

Partial melting of basaltic systems, especially at arc settings, often involves fluid components and/or more felsic lithologies (e.g., marine sediments and continental crust). The degree of such interaction can be inferred from U/Nb, Th/Nb ratios in zircon. Fluid immobile Nb fractionates from fluid mobile Th and U during low temperature surface weathering, erosion, and/or fluid interaction. Thus, normalization of Th and U to Nb can be used as a monitor for mixing with such exogenous materials.

Based on over 5300 zircon analyses compiled by Grimes et al. (2015)., the zircon formed in arc magmas may be distinguished from those derived from mid-ocean ridges and intraplate ocean island by notably higher U/Nb >20 and Th/Nb >10, due to the recycling of Th and U enriched sediments and/or contribution of U and Th mobilized by hydrous fluid. Therefore, zircon with U/Nb ≤ 20 and/or Th/Nb ≤ 10 best represent crystallization from mantle-equilibrated melt without sufficient interaction to surface materials and fluids.

Similar trace element systematics for assessing fluid interaction and felsic material assimilation include U/Yb and Th/Yb (Grimes et al., 2007). These proxies could be used interchangeably or considered as additional criteria to reaffirm the selection. However, the specific values of these ratios vary if source melt originate from variably enriched mantle sources. For example, while low U/Yb (< ~ 0.1) appears to be diagnostic of zircon from differentiated melt originating from a depleted mantle source, zircon from relatively enriched geochemical reservoirs typically carry higher U/Yb ratios (Grimes et al., 2007, Grimes et al., 2015, Carley et al. 2014). Therefore, while U/Nb and Th/Nb are preferred in this study, multiple filtering criteria are encouraged to be used simultaneously.

3.3 Zircon saturation context

As a magma progressively differentiates prior to zircon saturation, the precipitation of major mineral phases will continuously change the availability of major elements in the melt, including redox-sensitive ratios such as Fe^{2+}/Fe^{3+}, thereby manipulating the melt redox state. Saturation and/or dissolution of accessory phases, such as monazite or xenotime, can control trace element budgets in residual melts, thus changing the REE signatures inherited by zircon. In addition, the speed of magma differentiation and oversaturation of trace elements can lead to disequilibrium crystallization of zircon, resulting in observed partitioning behavior that deviate from calibrated relationships (e.g., Eqn (1)). Such magmatic processes play significant roles in changing melt redox states and influencing trace element concentrations in zircon. Beyond saturation from magmatic melt, zircon can also experience re-equilibration, dissolution, and recrystallization in Zr-rich melts sources from the decomposition of Zr-rich mineral phases, or Zr-rich metasomatic fluids. In such cases, saturation of non-magmatic zircon will not appropriately record the melt redox state via Eqn (1). We employ five chemical filters to monitor for: (1) fractionation of redox-sensitive mineral phases and REE-enriched accessory phases; (2) degree of magma differentiation; (3) equilibrium crystallization of zircon; and, (4) non-magmatic zircon signatures.

3.3.1 Absence of flat HREE pattern: $(Lu/Gd)_N$ between 10 and 74

The partitioning of heavy REE (HREE) zircon is suppressed due to fractionation of garnet prior to or contemporaneous with zircon crystallization, leading to a characteristic flat HREE pattern (or a "plateau") in the zircon. More problematic, the fractionation of garnet can alter the melt redox state by up to 6 orders of magnitude in arc settings (Tang et al., 2018), as Fe^{2+} is more compatible in garnet, leaving behind residual melt with a disproportionate concentration of Fe^{3+}. Because Fe serves as a major control on local fO_2, an increase in $Fe^{3+}/\Sigma Fe$ in the residual melt (as promoted by fractionation of garnet) could effectively oxidize the system, consequently changing the Ce^{4+}/Ce^{3+} ratio in the melt relative to the original mantle setting. In addition, flat HREE patterns may also be imparted by metamorphic processes. Under high-temperature and high-pressure environments where garnet is stable, partial melting or decomposition of Zr-rich mineral phases (e.g., titanite) can contribute Zr, leading to subsolidus crystallization of zircon. Similarly, zircon in mantle-derived host rocks devoid of garnet (i.e., kimberlite, carbonatite) can also have flat HREE pattern due to incomplete melting of garnet in mantle source region (Hoskin and Schaltegger, 2003; Rubatto, 2017). Saturation of zircon in mantle-derived melt is thermodynamically hindered unless it is aided by a large amount of metasomatic fluids or slab-derived felsic melt. Therefore, zircon with flat HREE pattern often associate fractionation of garnet in melt, metamorphic origin of zircon, or disequilibrium crystallization in mantle-derived host rock, so they imply little about the local magmatic environment.

Experimental results show that $D_{Lu}^{Zircon/Melt}/D_{Gd}^{Zircon/Melt}$ in hydrous granitic melt is approximately 15 at 800℃ and 20 kbar, typical conditions for subduction zone or thickened oceanic crust, but the value of this ratio diminishes to 11 in the presence of garnet (Rubatto and Hermann, 2007). During high temperature metamorphism in the lower crust (<900C, 7 kbar), $D_{Lu}^{Zircon/Garnet}/D_{Gd}^{Zircon/Garnet}$ further approaches unity (Taylor et al., 2015). This agrees with the empirical observations that mantle-affinity zircon (co-presence of garnet) have $(Lu/Gd)_N$ ranging from 1~10, metamorphic zircon with $(Lu/Gd)_N$ approaching 1 (Kelly and Harley, 2005; Whitehouse and Platt, 2003), whereas typical granitic zircon have $(Lu/Gd)_N$ ranging from 16-74 (Hoskin and Schaltegger, 2003). The formation of metamorphic zircon from garnet break-down during magma ascent also leads to a greater enrichment of HREE compared to magmatic zircon (Rubatto, 2002; El-Bialy and Ali, 2013). Therefore, magmatic zircon without coexistence of garnet tends to have $(Lu/Gd)_N$ between 10 and 74.

3.3.2 Avoiding fractionation of accessory phases: Th/U ratio between 0.2 and 4

Prior to or during zircon saturation, crystallization of Th-enriched phases (e.g., monazite and thorite) and/or U-enriched phases (e.g., coffinite, uraninite, or monazite) induces local heterogeneity of Th and U in the melt, enhancing observed Th/U variances in cogenetic magmatic zircon. Such heterogeneity can be further augmented via post-magmatic processes, such as hydrothermal alteration, metamorphism, and/or low temperature weathering. Hydrothermal fluids may mobilize, redistribute, or precipitate Th-rich and U-rich inclusions along cracks, or promote mass loss of U by oxidizing U^{4+} to form fluid mobile UO_4^{2-}. Metamorphism, decomposition, and crystallization of Th- and U-rich accessary phases can also incur spatial variations in Th and U concentration in melts, facilitating the dissolution and disequilibrium growth of zircon (Xiang et al., 2011). As a result, zircon with extreme values of Th/U are often associated with significant inclusion/fractionation of accessory phases, disequilibrium crystallization, and non-magmatic origins.

Based on 10,693 magmatic zircon analyses compiled in Kirkland et al. (2015), zircon Th/U ratios range from near 0 up to 19.8, with a median of 0.65 and a positive skewness of 6.7. Although metamorphic zircon exhibit a similar spread in Th/U, a greater percentage of metamorphic zircon have Th/U < 0.1 (Yakymchuk et al., 2018). Historically, Th/U < 0.1 was used as filtering tool for metamorphic zircon, but

even zircon in ultrahigh temperature metamorphic assemblage (> 900 ℃) can exhibit Th/U > 0.1, reinforcing the complexity of Th/U systematics (Kelly and Harley, 2005).

The large variance in Th/U recorded by natural zircon may be attributed to reasons mentioned above. However, the effects of each of these controls on Th/U ratios have not been fully characterized. Therefore, the Th/U ratio of the mantle is used to identify zircon that have preserved the native mantle signature. Assuming Th/U in the mantle varies between 0.2 to 4 (Wipperfurth et al., 2018), our dataset implies greater than 89% of zircon fall within this range (Figure 5).

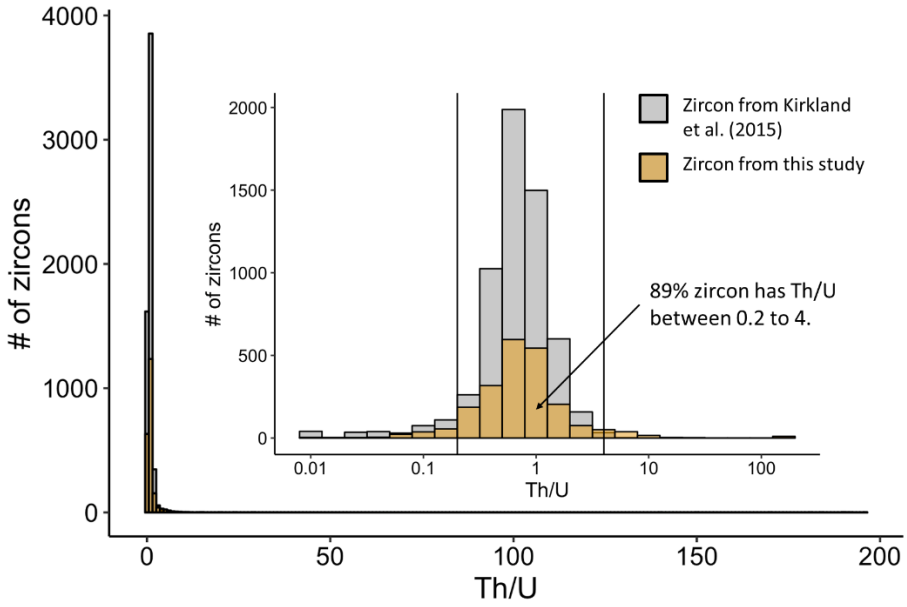

Figure 5. The distribution of Th/U ratio in the compiled dataset (n=2173) from this study and zircon from Kirkland et al. (2015). The insect shows the same plot in log scale.

3.3.3 Constraining differentiation and metasomatism: Hf concentration: 5,000-13,000 ppmw

As HFSE, Hf and Zr are both highly incompatible in most mineral phases, so the Hf and Zr concentration in melt increases significantly as magma differentiates. Zircon, as one of the primary carriers of Hf in magmatic systems, readily incorporates Hf into its crystal lattice due to the same valence states and similar ionic radii to Zr^{4+} (Wang et al., 2010). Therefore, the Zr/Hf ratio in zircon remains relatively constant in granitic magma unless metasomatism and/or crystallization of Hf-enriched accessary phases (e.g., hafnon) fractionate Zr/Hf.

According to 2201 zircon electron microprobe analyses complied in Wang et al. (2010), the Zr/Hf signatures recorded by granitic zircon range from 5 to 100, showing a nearly normal distribution with a mean, median, and mode of 39. Zircon from pegmatite or highly evolved rocks tend to have Zr/Hf closer to 20 (Linnen and Keppler, 2002; Pupin, 2000). Interactions with a fluid phase will reduce Zr/Hf ratio in zircon, resulting in enrichment and positive correlation between Hf and Rb (Linnen and Keppler, 2002).

By assuming an average Zr concentration in zircon based on stoichiometry, a Zr/Hf ratio between 39 (the mean/median/mode of granitic zircon) and 100 (the max value observed in the same data set; Wang et al., 2010) equates to 5,000 to 13,000 ppmw Hf in magmatic zircon. Approximately 85% of the data compiled in this study fall within this compositional range. Notably, zircon with Hf > 13,000 ppmw commonly exhibit higher La contents, corroborating a potential metasomatic influence and/or precipitation of LREE-enriched mineral phases.

3.3.4 Equilibrated crystallization of zircon from silicic melt: Eu/Eu*: 0.1 - 0.6

Besides Ce, Eu is another REE that has two valence states, Eu^{2+} and Eu^{3+}; Eu^{2+} is strongly incompatible in the zircon structure due to the large ionic size and required coupled substitution in zircon structure. Therefore, the Eu/Eu* ratios in zircon rarely exceed one, unless zircon saturates in disequilibrium conditions (Hoskin and Schaltegger, 2003; Trail et al., 2012).

The relationship between Eu/Eu* and Hf depicts a continuum of magma differentiation that connects zircon from mantle-derived melts (i.e., carbonatite and kimberlite) to silicic melt (i.e., igneous rocks; Figure 6). Majority of zircon in carbonatite and kimberlite are observed to have low Hf concentration and Eu/Eu* > 1, supporting hypothesis that saturation of zircon in mantle-derived melt is thermodynamically unfavorable. However, as magma sufficiently evolves, zircon inherits a higher concentration of Hf and lower Eu/Eu*; for example, the majority of igneous zircon from this study have Eu/Eu* $\prec$ 0.6 (Figure 6). The distribution of Eu/Eu* broadly correlates to types of parental magma. Zircon from I type granitoid has a distinctive lower En/Eu* $\leq$ 1 than zircon from S- and A-type granitoid (Wang et al., 2012; Sawaki et al., 2017). Therefore, mantle-equilibrated zircon is expected to have Eu/Eu* between 0.1 to 0.6.

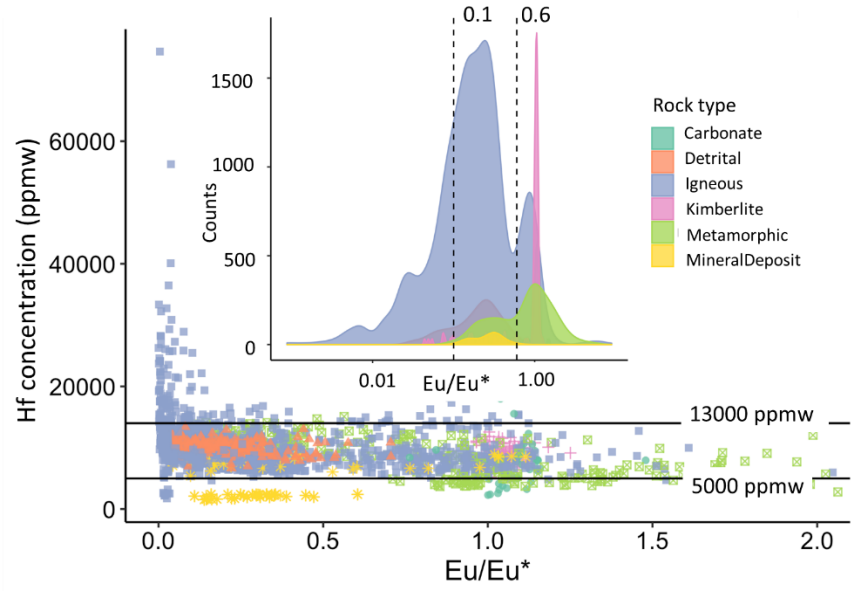

Figure 6. Hf concentration as a function of Eu/Eu* of zircon compiled in this study, categorized by host rock type. The inset shows the count distribution of Eu/Eu* of zircon by rock type.

3.3.5 Crystallization temperature for magmatic zircon: Ti concentration: 2 - 24 ppm

The onset temperature of zircon saturation is controlled by the compatibility of Zr in major mineral phases as they precipitate from a melt, and the starting Zr concentration of the system. By assuming a highly incompatible behavior of Zr in the phases that first crystallize from a basaltic magma ($D_{Zr} \leq 0.01$) and a 100 ppmw initial Zr concentration, zircon is expected to saturate starting at 850 °C based on simulation of magma differentiation (Lee et al., 2014; Nandedkar et al., 2014; Borisov, 2019). The actual zircon saturation temperature of 11,705 igneous zircon is estimated to be ~800 to 600 °C, based on their Ti concentration and melt composition parameter M (i.e., the cation ratio of (Na + K + 2Ca) / (Al·Si) of the melt/whole rock) (Samperton et al., 2017; Siégel et al., 2018).

The majority of zircon data compiled in this study has Ti-in-zircon temperatures between 710 and 810 °C, which converges to the crystallization temperature range suggested by the simulations described above, 600 to 850 °C as well as in literatures (Figure 7; Harrison et al., 2007; Fu et al., 2008). Therefore, by assuming unity a_{SiO_2} and a_{TiO_2} in Ti-in-zircon thermometry, we constrained the Ti concentration in magmatic zircon between 2 and 24 ppm, corresponding to zircon saturation temperature between 600 °C to 850 °C respectively.

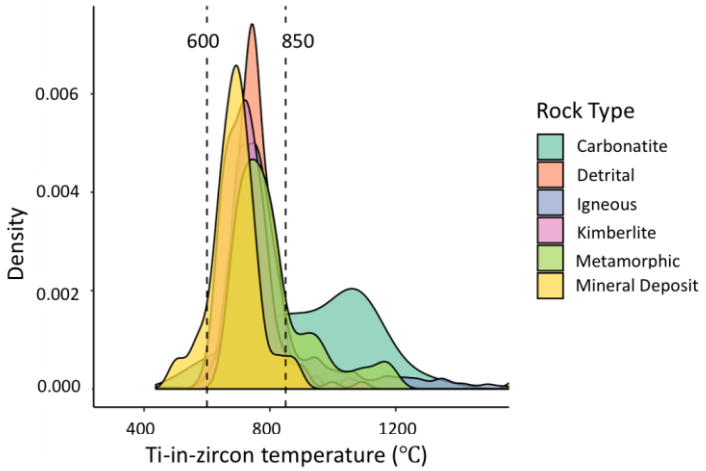

Figure 7. Density plot of Ti-in-zircon temperatures determined from the zircon data set compiled here, categorized by host rock type. The area under each curve has a cumulative probability of 1.

4. A proposed scoring system to gauge confidence

Based on the discussion above, a total of 13 filtering criteria are summarized, all of which help to limit external interferences and artificial variances in inferred redox states from three perspectives:

(1) Mineral inclusions in zircon:
La concentration: 0.002 - 0.1 ppm
$(Sm/La)_N$ between 100 and 1000

LREE_I > 60

(2) Source melt petrogenesis:

U/Nb ≤ 20

Th/Nb ≤ 10

P ≤ 750 ppmw and (REE+Y)/P molar ratio > 1

(3) Zircon saturation context:

Ce/Ce* ≤ 100

$(Lu/Gd)_N$ between 10 and 76

Hf concentration between 5000 and 13000 ppm

Th/U ratio between 0.2 and 4

Eu/Eu* between 0.1 to 0.6

Ti concentration between 2 to 24 ppm

These criteria may be translated into a numeric scheme by employing a binary scoring system. A zircon will score 1 for each criterion it satisfies in Categories (2) and (3); if the zircon falls outside the predefined range, it receives a score of 0 for that proxy. However, because inclusion phases have extraordinary control on both Ce/Ce* and Ti-in-zircon temperatures, the criteria outlined in Category (1) are given a 2x weight factor; that is to say, a zircon will receive a score of 2 for each criterion it satisfies in Category (1). If the zircon falls outside the predefined range, it receives a score of 0 for that Category (1) proxy. For example, a zircon entry that satisfies all criteria except that its U/Nb > 20, La concentration > 0.1 ppmw, and $(Lu/Gd)_N$ < 10 ppmw will have a total score of 11 (Figure 8).

The total score estimates the similarity of a given zircon entry to a mantle-equilibrated zircon. Zircon with the high scores are most likely to represent mantle-equilibrated zircon, whereas zircon with low scores have a reduced probability of preserving the identities of their respective mantle sources. Samples with the highest confidence of reflecting mantle-equilibrated zircon will have a maximum score of 15 (i.e., satisfying all criteria).

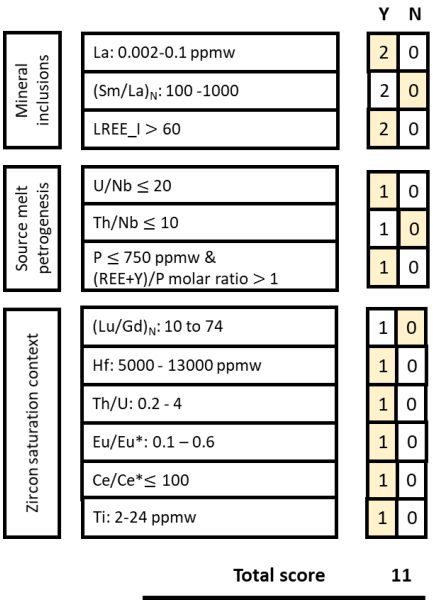

Figure 8. An example of calculating the score of zircon that satisfy all criteria except that its U/Nb $>$ 20, La concentration $>$ 0.1 ppmw, and $(Lu/Gd)_N < 10$.

5. Discussion

The scores for all 2173 zircon entries compiled here cover the entire scoring range from 1 to 15 (Figure 9). Application of Hoskin's differentiation diagrams suggest that most low score zircon are derived from hydrothermal sources, whereas high score zircon cluster within the magmatic domain (Figure 10). In general, the zircon population with the highest scores converge at melt redox states near the FMQ region. Based on the distributions of scores, the zircon may be divided into three groups, as described further below (Figure 11a).

5.1 Variation in inferred fO_2 due to magmatic and post-magmatic processes

Group III zircon have scores ≤ 7 with a median oxygen fugacity ΔFMQ -5.6 $\pm$ 5.1 ($\pm$ median absolute deviation; Fig. 11a). Consequently, these samples are interpreted to represent non-magmatic zircon. The median absolute deviation is calculated as the median of the absolute distances of each data value to the median of whole sample set; compared to standard deviations, this value is less affected by outliers and better represents statistical dispersion within dataset. Group III zircon generally yield Ce/Ce* approaching unity but surprisingly high Ti-in-zircon temperatures (>1000 ℃), highlighting unusual trace element characteristics (Figure 9). Group III zircon represent >75 % of zircon from metamorphic rocks and > 90% from carbonatites (Figure 11b). According to the textures and morphologies of these samples provided in their source references, zircon with unity Ce/Ce* and high temperature often associates with metamict, hydrothermal, and metamorphic zircon, which validate that Group III zircon represent non-magmatic origin (Figure 12).

Group II zircon have scores from 8 to 13 with a median oxygen fugacity ΔFMQ -0.3 $\pm$ 4.8. They mostly represent zircon with mineral inclusions and zircon that crystallized from parental magma that interacted with hydrous fluids and/or crustal materials. Group II zircon have Ti-in-zircon temperature 620 to 850 ℃, in agreement with experiments and simulations of magmatic zircon crystallization temperature. However, their Ce/Ce* ranges over three orders of magnitudes (Figure 9). Hoskin discriminant diagrams suggest the majority of Group II zircon extend from the magmatic zone towards hydrothermal signatures (Figure 10). Such a trend implies that Group II zircon may have had magmatic origins but fluid alteration and/or metamorphism conditions induced post-magmatic trace element diffusion, mineral exsolution, or inclusions that attenuated Ce/Ce* and diminish the original magmatic fingerprint.

Group II includes nearly all zircon derived from kimberlites, detrital zircon in sedimentary rocks (i.e., siltstone), and ~40% zircon from igneous rocks (Figure 11b). According to the specific examples in this study, zircon in kimberlite is identified as xenocryst with a source melt of mafic composition (Kostrovitsky et al., 2016), and detrital zircon in siltstone is crystalized from a melt of A-type granitoid or a mixture of felsic and mafic melt (Paulsen et al., 2017). Therefore, despite the range of host rock compositions, most of Group II zircon have a magmatic origin. Petrographic examination via BSE and CL images suggest most Group II samples have magmatic textures but with inclusions or secondary recrystallization features, likely resulting from hydrothermal fluids or metamorphism (Figure 12).

Group I zircon have scores from 14 to 15, meaning they have the highest confidence level of representing mantle-equilibrated zircon. The most noticeable differences between Group I and II zircon

564 are the reduced variations in temperature and Ce/Ce*, and by extension inferred melt redox state (Figure
565 11a).

566 The majority of Group I zircon are from the rhyolitic Mesa Falls Tuff (MFT) at Yellowstone volcanic
567 field (Rivera et al., 2016). The physical conditions and mechanisms of generating silicic magma at
568 Yellowstone are hotly debated topics because cyclic caldera collapse, magma mixing, and crustal
569 assimilation often overprint and complicate the signatures of minerals and magma (Bindeman and Valley,
570 2001; Wotzlaw et al., 2015). As a result, Yellowstone zircon often inherit heterogeneous oxygen isotopic
571 compositions and trace element concentrations across zones that reflect variations in melt conditions as a
572 function of time. Based on detailed petrographic observation, trace element composition, and U-Pb dating,
573 Rivera et al. (2016) identified 4 Chemical Domains in MFT zircon that represent distinctive magma
574 conditions; in general, Domains 1 and 2 represent magma mixing from hydrothermally altered crust
575 (characterized by statistically distinct $\delta^{18}O$ below mantle field); Domain 3 represents the oldest pristine
576 magma in the zircon core; and, Domain 4 represents magma with significant fractionation. Out of >400
577 zircon analyses, this filter scheme has successfully avoided all zircon from Domains 1, 2, and 4, and only
578 picked up zircon from Domain 3, sourced from the most primitive melt. Similarly, other Group I zircon
579 include magmatic cores from Cu-Zn deposits (Zhu et al, 2017), detrital zircon in siltstone (Paulsen, 2017),
580 and magmatic zircon from Yellowstone rhyolite (Colon et al., 2015). Although there are no oxygen
581 isotopes for selected zircon grains as corroborative validation for their mantle-equilibrated source melt, all
582 of these references have: (1) observed multistage growth of zircon and preservation of magmatic texture
583 for some zircon; and, (2) highlighted the likelihood of maintaining mantle-equilibrated source melt based
584 on Hf and oxygen isotopes on limited zircon grains and whole rock.

585 Accordingly, this filter scheme has demonstrated the capacity to isolate non-magmatic zircon (Group III
586 zircon), magmatic zircon with inclusions or enriched source melt sources (Group II zircon), and mantle-
587 equilibrated zircon (Group I). Based on the Group I zircon population from the compiled zircon dataset
588 interrogated here, we infer a local mantle redox state of ΔFMQ 2.56 ± 0.90 (n= 17). This result overlaps
589 with upper mantle redox values ΔFMQ $\pm$ 2 via $Fe^{3+}/\Sigma Fe$ on spinel peridotites (Frost and McCammon,
590 2008). Such variation could be a true variation of natural melt redox state, or due to uncertainty of trace
591 element measurements. The main sources of uncertainty of this inferred redox state are: (1) unfiltered
592 inclusions; (2) variable source melt sources and compositions (and potential magma mixing); (3) extreme
593 fractional crystallization; (4) analytical uncertainty in trace element measurements; and, (5) inaccuracy of
594 the melt redox state calculation (Eqn. 1).

595

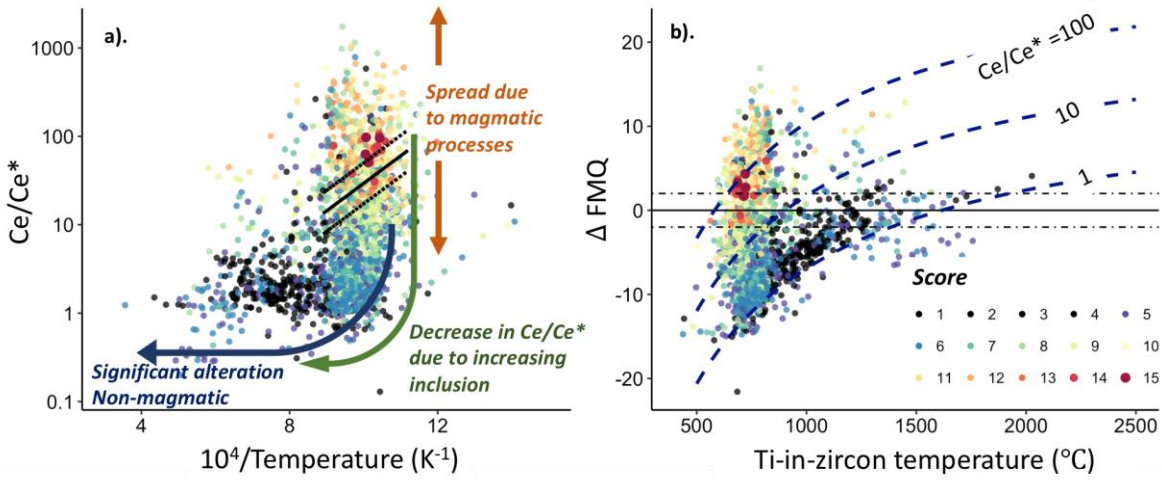

596

597 **Figure 9.** Application of the proposed filter scheme and scoring system to the zircon dataset compiled
598 here (n = 2173). In general, the large spread in observed Ce/Ce* may be attributed to distinct sources of
599 source melts, magmatic differentiation prior to zircon saturation, and/or mineral inclusions in trace
600 element measurements. The black dotted and solid lines represent ΔFMQ±2, and blue dashed lines
601 represent ΔFMQ of a single Ce/Ce* value at different Ti-in-zircon temperatures.

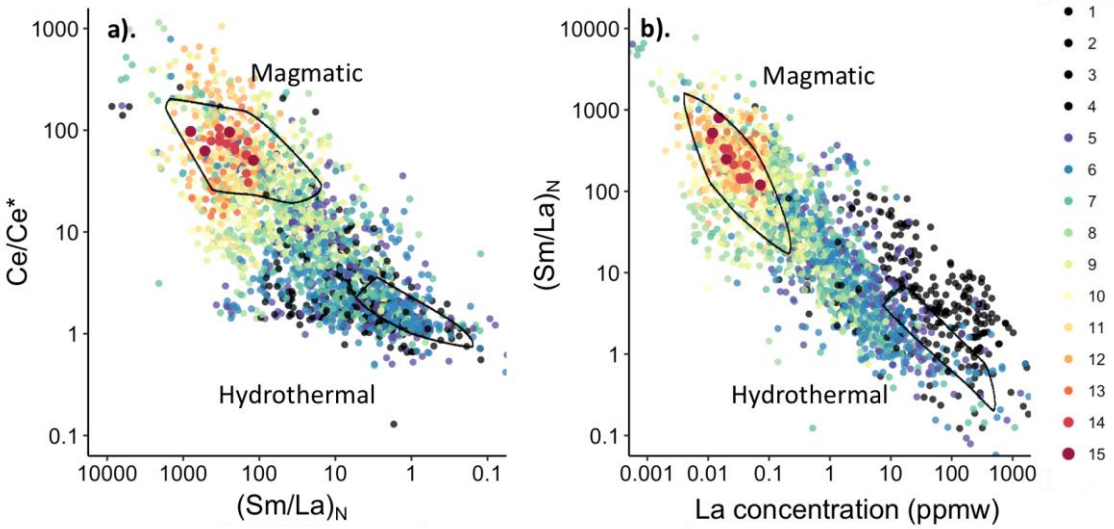

602

603 **Figure 10.** Distribution of the compiled zircon data set within the pre-established magmatic and
604 hydrothermal fields proposed by Hoskin (2005).

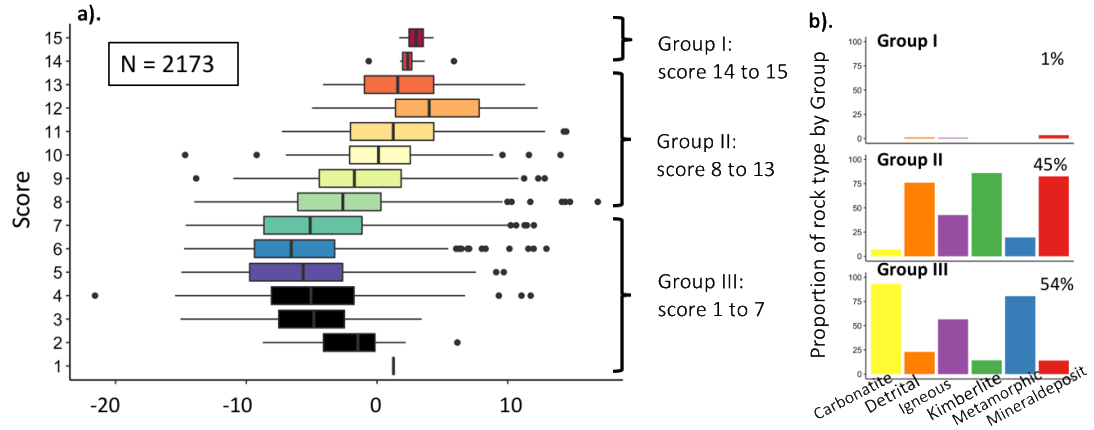

605

606 **Figure 11.** (a) Boxplots of zircon populations for each score. Based on the median and variance of
607 inferred melt redox states, these populations may be divided into three groups: Group I (score 14 to 15),
608 Group II (score 8 to 13), and Group III (score 1 to 7). (b) Selectivity and distribution of different rock
609 types within each group (the percentage represents the proportion of all zircon that fall within each group).

610

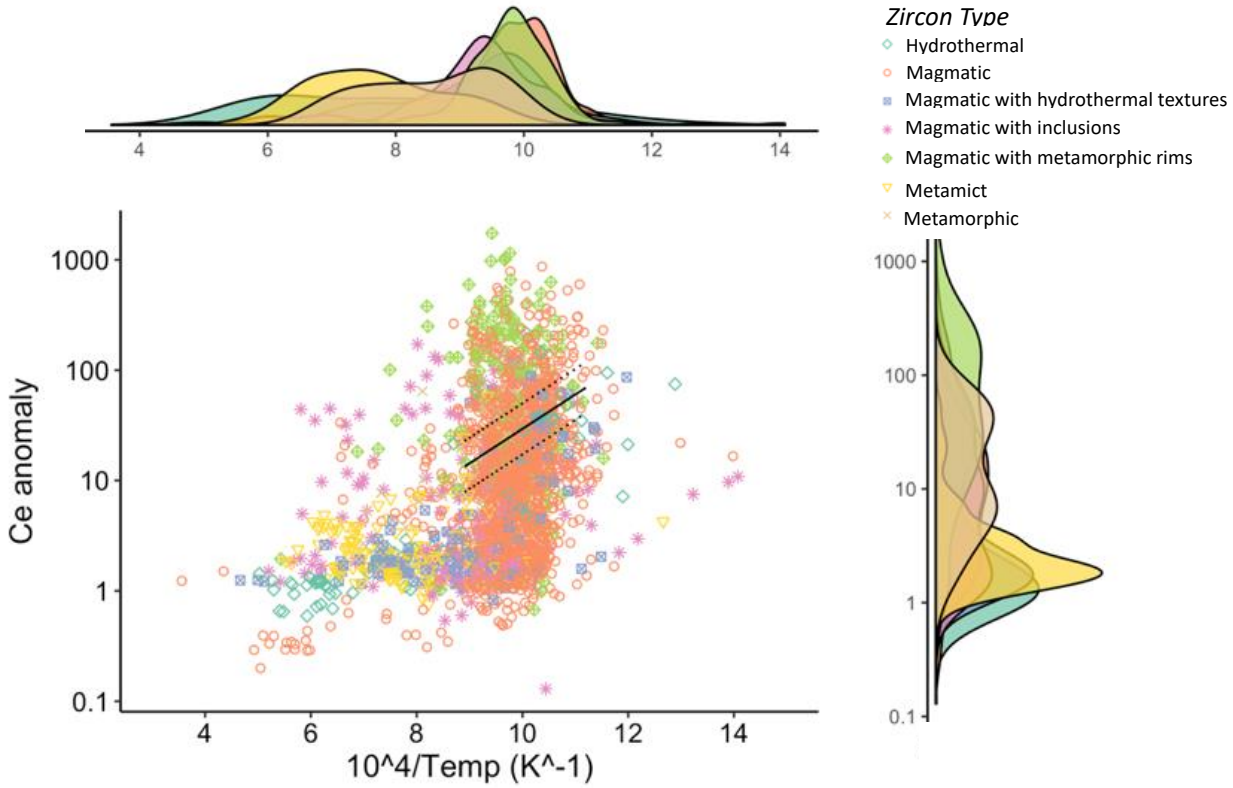

611
612 **Figure 12.** Plot of Ce/Ce* and temperature in zircon as a function of morphology and textures. The
613 texture of each individual zircon was deduced from BSE and CL imaging from source references (see
614 Supplementary Material I for more details). The black dotted and solid lines represent ΔFMQ±2.

615 **5.2 Application: a case study of TTG zircon from Greenland**

A case study of 76 zircon from three Tonalite-Trondhjemite-Granodiorite (TTG) rock samples (524994, 524906, 524907) in Greenland is considered here using the filter scheme described above. The trace elements in each sample were measured via laser ablation inductively coupled plasma mass spectrometry (LA-ICPMS; see Supplementary Material III). After calculating inferred oxygen fugacity (via Ce/Ce*) and Ti-in-zircon temperatures using Eqn (1) and (2), assuming unity for a_{SiO_2} and a_{TiO_2}, the score of each zircon grain was determined (Figure 13).

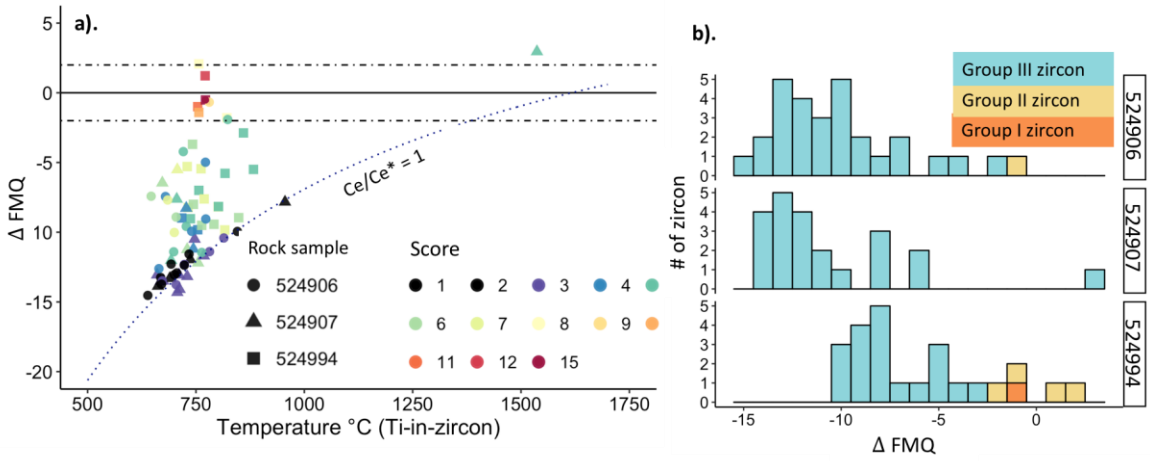

Figure 13. Application of the filter scheme proposed here to a case study of TTG zircon from three independent samples (524906, 524907, 524994) from Greenland (see Supplementary Material II for location). (a) Inferred melt redox state as a function of temperature. (b) Distribution of zircon by group.

According to the distribution of scores, most zircon in these three Greenland rock samples may be characterized as Group III, suggesting a non-magmatic origin (Figure 13b). However, the presence of all three classes of zircon (Groups I, II, and III) implies a multi-stage zircon saturation in the host rocks. Although a few zircon in 524994 retained their magmatic signatures (Group I samples), the majority has experienced significant degrees of hydrothermal alterations and/or metamorphism that led to either recrystallization as non-magmatic zircon (Group III) or intermediate degrees of modification (Group II). By using the trace element composition of the highest score zircon grain (the most likely mantle-equilibrated candidate), we infer a local melt redox state of ΔFMQ -0.5 ca. 2950 Ma. Again, such result agrees with the inferred redox state of upper mantle redox via other proxies (ΔFMQ $\pm$ 2, Frost and McCammon, (2008)), which imply the validity of assuming unity a_{SiO_2} and a_{TiO_2} to estimate Ti-in-zircon temperature of mantle-equilibrated zircon.

In summary, this filter scheme not only provides quick insights about of zircon saturation, petrogenesis of zircon textures and morphology, and source melt conditions, but also accelerates research by prioritizing magmatic zircon crystals that are least likely to be contaminated, or chemically overprinted. Other obvious applications of this filter scheme include studies of both out-of-context and in-context zircon, providing a quick guideline for directing more comprehensive and lab-intensive whole rock, imaging, and isotopic investigations.

6. Conclusions

We have established a simple filter scheme for selecting of mantle-equilibrated zircon using only trace element systematics (P, Ti, Y, Nb, REE, Hf, Th, U) as a way to circumvent more extensive analytical meausrements/techniques when time, access to lab facilities, and financial resources are limited. This filter scheme has demonstrated the capability of isolating non-magmatic zircon (Group III scores ≤ 7), magmatic zircon with inclusions or derived from enriched source melt (Group II scores between 8 and 13), and mantle-equilibrated zircon (Group I score ≥ 14). The causes of variation in inferred redox states Include: (1) unfiltered inclusions; (2) distinct source melt sources and potential magma mixing; (3) variable degrees of magma differentiation; (4) analytical uncertainty in trace element measurements; and, (5) inaccuracy of the melt redox state calculation. Despite these uncertainties, mantle-disequilibrated zircon are effectively identified without requiring traditional protocols (i.e., petrographic studies, whole rocks analysis, and oxygen isotopes), enabling the derivation of local mantle oxygen fugacity from trace element measurements alone. The selected mantle-equilibrated zircon from a case study of Greenland TTG zircon using this filter scheme implicate a mantle source ΔFMQ -0.5 ca. 2950 Ma.

Although this filter scheme cannot provide zircon analysis as thorough as more comprehensive protocols, it provides quick insights about petrogenesis of zircon, including zircon saturation, textures, and morphology, and source melt conditions. The filtering criteria also accelerate research by prioritizing magmatic zircon crystals that are least likely to be chemically overprinted. Future applications of this filter scheme extend to studies of out-of-context and in-context zircon.

References

1. Anderson, A., Wirth, R., & Thomas, R. (2008). The alteration of metamict zircon and its role in the remobilization of high-field-strength elements in the Georgeville granite, Nova Scotia. *Canadian Mineralogist*, *46*(1), 1–18. https://doi.org/10.3749/canmin.46.1.1
2. Arevalo, R., & McDonough, W. F. (2010). Chemical variations and regional diversity observed in MORB. *Chemical Geology*, *271*(1–2), 70–85. https://doi.org/10.1016/j.chemgeo.2009.12.013
3. Bea, F. (1996). Residence of REE, Y, Th and U in granites and crustal protoliths; implications for the chemistry of crustal melts. *Journal of Petrology*, *37*(3), 521–552. https://doi.org/10.1093/petrology/37.3.521
4. Bell, E. A., Boehnke, P., Barboni, M., & Harrison, T. M. (2019). Tracking chemical alteration in magmatic zircon using rare earth element abundances. *Chemical Geology*, *510*, 56–71. https://doi.org/10.1016/j.chemgeo.2019.02.027
5. Bell, E. A., Boehnke, P., Hopkins-Wielicki, M. D., & Harrison, T. M. (2015). Distinguishing primary and secondary inclusion assemblages in Jack Hills zircons. *Lithos*, *234–235*, 15–26. https://doi.org/10.1016/j.lithos.2015.07.014
6. Belousova, E. A., Griffin, W. L., O'Reilly, S. Y., & Fisher, N. I. (2002). Igneous zircon: Trace element composition as an indicator of source rock type. *Contributions to Mineralogy and Petrology*, *143*(5), 602–622. https://doi.org/10.1007/s00410-002-0364-7
7. Bindeman, I. N., & Valley, J. W. (2001). Low-δ18O Rhyolites from Yellowstone: Magmatic evolution based on analyses of zircons and individual phenocrysts. *Journal of Petrology*, *42*(8), 1491–1517. https://doi.org/10.1093/petrology/42.8.1491
8. Boehnke, P., Watson, E. B., Trail, D., Harrison, T. M., & Schmitt, A. K. (2013). Zircon saturation re-revisited. *Chemical Geology*, *351*, 324–334. https://doi.org/10.1016/J.CHEMGEO.2013.05.028

9. Borisov, A., & Aranovich, L. (2019). Zircon solubility in silicate melts: New experiments and probability of zircon crystallization in deeply evolved basic melts. *Chemical Geology*, *510*, 103–112. https://doi.org/10.1016/j.chemgeo.2019.02.019
10. Burnham, A. D., & Berry, A. J. (2012). An experimental study of trace element partitioning between zircon and melt as a function of oxygen fugacity. *Geochimica et Cosmochimica Acta*, *95*, 196–212. https://doi.org/10.1016/j.gca.2012.07.034
11. Burnham, A. D., & Berry, A. J. (2017). Formation of Hadean granites by melting of igneous crust. *Nature Geoscience*, *10*(6), 457–461. https://doi.org/10.1038/ngeo2942
12. Carley, T. L., Miller, C. F., Wooden, J. L., Padilla, A. J., Schmitt, A. K., Economos, R. C., Bindeman, I. N., Jordan, B. T. (2014). Iceland is not a magmatic analog for the Hadean: Evidence from the zircon record. *Earth and Planetary Science Letters*, *405*, 85–97. https://doi.org/10.1016/j.epsl.2014.08.015
13. Chapman, J. B., Gehrels, G. E., Ducea, M. N., Giesler, N., & Pullen, A. (2016). A new method for estimating parent rock trace element concentrations from zircon. *Chemical Geology*, *439*, 59–70. https://doi.org/10.1016/j.chemgeo.2016.06.014
14. Chou, M. (1978). Calibration of oxygen buffers at elevated P and T using the hydration fugacity sensor. *American Mineralogist*, *63*, 690–703.
15. Corfu, F., Hanchar, J. M., Hoskin, P. W. O., & Kinny, P. (2003). Atlas of Zircon Textures. *Reviews in Mineralogy and Geochemistry*, *53(1)*, 469–500. https://doi.org/10.2113/0530469
16. El-Bialy, M. Z., & Ali, K. A. (2013). Zircon trace element geochemical constraints on the evolution of the Ediacaran (600-614Ma) post-collisional Dokhan Volcanics and Younger Granites of SE Sinai, NE Arabian-Nubian Shield. *Chemical Geology*, *360–361*, 54–73. https://doi.org/10.1016/j.chemgeo.2013.10.009
17. Ferry, J. M., & Watson, E. B. (2007). New thermodynamic models and revised calibrations for the Ti-in-zircon and Zr-in-rutile thermometers. *Contributions to Mineralogy and Petrology*, *154*(4), 429–437. https://doi.org/10.1007/s00410-007-0201-0
18. Frost, D. J., & McCammon, C. A. (2008). The Redox State of Earth's Mantle. *Annual Review of Earth and Planetary Sciences*, *36*(1), 389–420. https://doi.org/10.1146/annurev.earth.36.031207.124322
19. Frost, D. J., Mann, U., Asahara, Y., & Rubie, D. C. (2008). The redox state of the mantle during and just after core formation. *Philosophical Transactions of the Royal Society A: Mathematical, Physical and Engineering Sciences*, *366*(1883), 4315–4337. https://doi.org/10.1098/rsta.2008.0147
20. Fu, B., Page, F. Z., Cavosie, A. J., Fournelle, J., Kita, N. T., Lackey, J. S., Wilde, S. A., Valley, J. W. (2008).Ti-in-zircon thermometry: Applications and limitations. *Contributions to Mineralogy and Petrology*, *156*(2), 197–215. https://doi.org/10.1007/s00410-008-0281-5
21. Gale, A., Dalton, C. A., Langmuir, C. H., Su, Y., & Schilling, J.-G. (2013). The mean composition of ocean ridge basalts. *Geochemistry, Geophysics, Geosystems*, *14*(3), 489–518. https://doi.org/10.1029/2012GC004334
22. Grimes, C. B., John, B. E., Kelemen, P. B., Mazdab, F. K., Wooden, J. L., Cheadle, M. J., Hanghøj, K., Schwartz, J. J. (2007). Trace element chemistry of zircons from oceanic crust: A method for distinguishing detrital zircon provenance. *Geology*, *35*(7), 643. https://doi.org/10.1130/G23603A.1

23. Grimes, C. B., Wooden, J. L., Cheadle, M. J., & John, B. E. (2015). "Fingerprinting" tectono-magmatic provenance using trace elements in igneous zircon. *Contributions to Mineralogy and Petrology*, *170*(5–6), 46. https://doi.org/10.1007/s00410-015-1199-3
24. Hanchar, J. M., & Watson, E. B. (2003). Zircon saturation thermometry. *Reviews in Mineralogy and Geochemistry*, *53*(1), 89–112. https://doi.org/10.2113/0530089
25. Harrison, T. M., Watson, E. B., & Aikman, A. B. (2007). Temperature spectra of zircon crystallization in plutonic rocks. *Geology*, *35*(7), 635–638. https://doi.org/10.1130/G23505A.1
26. Hawkesworth, C. J., & Kemp, A. I. S. (2006). Using hafnium and oxygen isotopes in zircons to unravel the record of crustal evolution. *Chemical Geology*, *226*(3–4), 144–162. https://doi.org/10.1016/j.chemgeo.2005.09.018
27. Hofmann, A. E., Baker, M. B., & Eiler, J. M. (2014). Sub-micron-scale trace-element distributions in natural zircons of known provenance: implications for Ti-in-zircon thermometry. *Contrib Mineral Petrol*, *168*, 1057. https://doi.org/10.1007/s00410-014-1057-8
28. Hoskin, P. W. O. (2005). Trace-element composition of hydrothermal zircon and the alteration of Hadean zircon from the Jack Hills, Australia. *Geochimica et Cosmochimica Acta*, *69*(3), 637–648. https://doi.org/10.1016/j.gca.2004.07.006
29. Hoskin, P. W. O., & Black, L. P. (2002). Metamorphic zircon formation by solid-state recrystallization of protolith igneous zircon. *Journal of Metamorphic Geology*, *18*(4), 423–439. https://doi.org/10.1046/j.1525-1314.2000.00266.x
30. Hoskin, P. W. O., & Ireland, T. R. (2000). Rare earth element chemistry of zircon and its use as a provenance indicator. *Geology*, *28*(7), 627–630. https://doi.org/10.1130/0091-7613(2000)028<0627:REECOZ>2.3.CO;2
31. Hoskin, P. W. O., & Schaltegger, U. (2003). The composition of zircon and igneous and metamorphic petrogenesis. *Reviews in Mineralogy and Geochemistry*, *53*(1), 27-62. https://doi.org/10.1046/j.1525-1314.2000.00266.x
32. Kelly, N. M., & Harley, S. L. (2005). An integrated microtextural and chemical approach to zircon geochronology: refining the Archaean history of the Napier Complex, east Antarctica. *Contributions to Mineralogy and Petrology*, *149*(1), 57–84. https://doi.org/10.1007/s00410-004-0635-6
33. Kirkland, C. L., Smithies, R. H., Taylor, R. J. M., Evans, N., & McDonald, B. (2015). Zircon Th/U ratios in magmatic environs. *Lithos*, *212–215*, 397–414. https://doi.org/10.1016/j.lithos.2014.11.021
34. Kosler, J., & Sylvester, P. (2005). Present trends and the future of zircon in geochronology: laser ablation ICPMS. *Reviews in Mineralogy and Geochemistry*, *53*(1), 243–275. https://doi.org/10.2113/0530243
35. Kump, L. R., Kasting, J. F., & Barley, M. E. (2001). Rise of atmospheric oxygen and the "upside-down" Archean mantle. *Geochemistry, Geophysics, Geosystems*, *2*(1), 1525-2027. https://doi.org/10.1029/2000gc000114
36. Lee, C. T. A., & Bachmann, O. (2014). How important is the role of crystal fractionation in making intermediate magmas? Insights from Zr and P systematics. *Earth and Planetary Science Letters*, *393*, 266-274. https://doi.org/10.1016/j.epsl.2014.02.044
37. Lee, C.-T. A., Luffi, P., Chin, E. J., Bouchet, R., Dasgupta, R., Morton, D. M., Roux, V. L., Yin, Q., Jin, D. (2012). Copper systematics in arc magmas and implications for crust-mantle differentiation. *Science*, *336*(6077), 64–68. https://doi.org/10.1126/science.1217313

38. Linnen, R. L., & Keppler, H. (2002). Melt composition control of Zr/Hf fractionation in magmatic processes. *Geochimica et Cosmochimica Acta*, *66*(18), 3293–3301. https://doi.org/10.1016/S0016-7037(02)00924-9
39. McCammon, C. (2005). GEOCHEMISTRY: The Paradox of Mantle Redox. *Science*, *308*(5723), 807–808. https://doi.org/10.1126/science.1110532
40. McDonough, W. F., & Sun, S. S. (1995). The Composition of the Earth. *Chemical Geology*, *120*(3–4), 223–253. https://doi.org/10.1016/0009-2541(94)00140-4
41. Mysen, B. O., Holtz, F., Pichavant, M., Beny, J. M., & Montel, J. M. (1997). Solution mechanisms of phosphorus in quenched hydrous and anhydrous granitic glass as a function of peraluminosity. *Geochimica et Cosmochimica Acta*, *61*(18), 3913–3926. https://doi.org/10.1016/S0016
42. Nandedkar, R. H., Ulmer, P., & Müntener, O. (2014). Fractional crystallization of primitive, hydrous arc magmas: An experimental study at 0.7 GPa. *Contributions to Mineralogy and Petrology*, *167*(6), 1–27. https://doi.org/10.1007/s00410-014-1015-5
43. Page, F. Z., Fu, B., Kita, N. T., Fournelle, J., Spicuzza, M. J., Schulze, D. J., … Valley, J. W. (2007). Zircons from kimberlite: New insights from oxygen isotopes, trace elements, and Ti in zircon thermometry. *Geochimica et Cosmochimica Acta*, *71*(15), 3887–3903. https://doi.org/10.1016/j.gca.2007.04.031
44. Pidgeon, R. T., Nemchin, A. A., Roberts, M. P., Whitehouse, M. J., & Bellucci, J. J. (2019). The accumulation of non-formula elements in zircons during weathering: Ancient zircons from the Jack Hills, Western Australia. *Chemical Geology*, *530*. https://doi.org/10.1016/j.chemgeo.2019.119310
45. Pupin, J.-P. (2000). Granite genesis related to geodynamics from Hf-Y in zircon. *Earth and Environmental Science Transactions of the Royal Society of Edinburgh*, *91*(1–2), 245–256. https://doi.org/10.1017/S0263593300007410
46. Rasmussen, B., Fletcher, I. R., Muhling, J. R., Gregory, C. J., & Wilde, S. A. (2011). Metamorphic replacement of mineral inclusions in detrital zircon from Jack Hills, Australia: Implications for the Hadean Earth. *Geology*, *39*(12), 1143–1146. https://doi.org/10.1130/G32554.1
47. Rubatto, D. (2002). Zircon trace element geochemistry: Partitioning with garnet and the link between U-Pb ages and metamorphism. *Chemical Geology*, *184*(1–2), 123–138. https://doi.org/10.1016/S0009-2541(01)00355-2
48. Rubatto, D. (2017). Zircon: The Metamorphic Mineral. *Reviews in Mineralogy and Geochemistry*, *83*(1), 261–295. https://doi.org/10.2138/rmg.2017.83.9
49. Rubatto, D., & Hermann, J. (2007). Experimental zircon/melt and zircon/garnet trace element partitioning and implications for the geochronology of crustal rocks. *Chemical Geology*, *241*(1–2), 38–61. https://doi.org/10.1016/j.chemgeo.2007.01.027
50. Rudnick, R. L. (1995). Making continental crust. *Nature*, *378*(6557), 571–578. https://doi.org/10.1038/378571a0
51. Samperton, K. M., Bell, E. A., Barboni, M., Brenhin Keller, C., & Schoene, B. (2017). Zircon age-temperature-compositional spectra in plutonic rocks. *Geology*, *45*(11), 983–986. https://doi.org/10.1130/G38645.1
52. Sawaki, Y., Suzuki, K., Asanuma, H., Okabayashi, S., Hattori, K., Saito, T., & Hirata, T. (2017). Geochemical characteristics of zircons in the Ashizuri A-type granitoids: An additional granite

topology tool for detrital zircon studies. *Island Arc*, *26*(6), e12216. https://doi.org/10.1111/iar.12216

53. Shao, T., Xia, Y., Ding, X., Cai, Y., & Song, M. (2019). Zircon saturation in terrestrial basaltic melts and its geological implications. *Solid Earth Sciences*, *4*(1), 27–42. https://doi.org/10.1016/j.sesci.2018.08.001
54. Siégel, C., Bryan, S. E., Allen, C. M., & Gust, D. A. (2018). Use and abuse of zircon-based thermometers: A critical review and a recommended approach to identify antecrystic zircons. *Earth-Science Reviews*, *176*, 87–116. https://doi.org/10.1016/J.EARSCIREV.2017.08.011
55. Smythe, D. J., & Brenan, J. M. (2015). Cerium oxidation state in silicate melts: Combined fO2, temperature and compositional effects. *Geochimica et Cosmochimica Acta*, *170*, 173–187. https://doi.org/10.1016/j.gca.2015.07.016
56. Smythe, D. J., & Brenan, J. M. (2016). Magmatic oxygen fugacity estimated using zircon-melt partitioning of cerium. *Earth and Planetary Science Letters*, *453*, 260–266. https://doi.org/10.1016/j.epsl.2016.08.013
57. Spandler, C., Hermann, J., & Rubatto, D. (2004). Exsolution of thortveitite, yttrialite and xenotime during low temperature recrystallization of zircon from New Caledonia, and their significance for trace element incorporation in Nanogranitoids and crustal melting View project Magma fertility for Au-Cu, petrogenesis and geodynamic setting of Carboniferous and Permian magmatic complexes (Queensland, Australia) View project. *American Mineralogist*, *89*, 1795–1806. https://doi.org/10.2138/am-2004-11-1226
58. Spencer, C. J., Cavosie, A. J., Raub, T. D., Rollinson, H., Jeon, H., Searle, M. P., … Evans, N. J. (2017). Evidence for melting mud in Earth's mantle from extreme oxygen isotope signatures in zircon. *Geology*, *45*(11), 975–978. https://doi.org/10.1130/G39402.1
59. Tang, M., Erdman, M., Eldridge, G., & Lee, C. T. A. (2018). The redox "filter" beneath magmatic orogens and the formation of continental crust. *Science Advances*, *4*(5). https://doi.org/10.1126/sciadv.aar4444
60. Taylor, R. J. M., Harley, S. L., Hinton, R. W., Elphick, S., Clark, C., & Kelly, N. M. (2015). Experimental determination of REE partition coefficients between zircon, garnet and melt: a key to understanding high-T crustal processes. *Journal of Metamorphic Geology*, *33*(3), 231–248. https://doi.org/10.1111/jmg.12118
61. Trail, D., Bruce Watson, E., & Tailby, N. D. (2012). Ce and Eu anomalies in zircon as proxies for the oxidation state of magmas. *Geochimica et Cosmochimica Acta*, *97*, 70–87. https://doi.org/10.1016/J.GCA.2012.08.032
62. Trail, D., Mojzsis, S. J., Harrison, T. M., Schmitt, A. K., Watson, E. B., & Young, E. D. (2007). c. *Geochemistry, Geophysics, Geosystems*, *8*(6). https://doi.org/10.1029/2006GC001449
63. Trail, D., Tailby, N., Wang, Y., Mark Harrison, T., & Boehnke, P. (2017). Aluminum in zircon as evidence for peraluminous and metaluminous melts from the Hadean to present. *Geochemistry, Geophysics, Geosystems*, *18*(4), 1580–1593. https://doi.org/10.1002/2016GC006794
64. Trail, D., Watson, E. B., & Tailby, N. D. (2011). The oxidation state of Hadean magmas and implications for early Earth's atmosphere. *Nature*, *480*(7375), 79–82. https://doi.org/10.1038/nature10655
65. Valley, J. W. (2003). Oxygen Isotopes in Zircon. *Reviews in Mineralogy and Geochemistry*, *53*(1), 343–385. https://doi.org/10.2113/0530343

66. Valley, J. W., Kinny, P. D., Schulze, D. J., & Spicuzza, M. J. (1998). Zircon megacrysts from kimberlite: oxygen isotope variability among mantle melts. *Contributions to mineralogy and petrology*, *133*(1-2), 1-11. https://doi.org/10.1007/s004100050432
67. Wang, Q., Zhu, D. C., Zhao, Z. D., Guan, Q., Zhang, X. Q., Sui, Q. L., Hu, Z. C., Mo, X. X. (2012). Magmatic zircons from I-, S- and A-type granitoids in Tibet: Trace element characteristics and their application to detrital zircon provenance study. *Journal of Asian Earth Sciences*, *53*, 59–66. https://doi.org/10.1016/j.jseaes.2011.07.027
68. Wang, X., Griffin, W. L., & Chen, J. (2010). Hf contents and Zr/Hf ratios in granitic zircons. *Geochemical Journal*, *44*(1), 65–72. https://doi.org/10.2343/geochemj.1.0043
69. Watson, E. B. (1979). Zircon saturation in felsic liquids: Experimental results and applications to trace element geochemistry. *Contributions to Mineralogy and Petrology*, *70*(4), 407–419. https://doi.org/10.1007/BF00371047
70. Watson, E. B., & Harrison, T. M. (1983). Zircon saturation revisited: temperature and composition effects in a variety of crustal magma types. *Earth and Planetary Science Letters*, *64*(2), 295–304. https://doi.org/10.1016/0012-821X(83)90211-X
71. Watson, E. B., & Harrison, T. M. (2005). Zircon Thermometer Reveals Minimum Melting Conditions on Earliest Earth. *Science*, *308*(5723), 841–844. https://doi.org/10.1126/science.1110265
72. Watson, E. B., Wark, D. A., & Thomas, J. B. (2006). Crystallization thermometers for zircon and rutile. *Contributions to Mineralogy and Petrology*, *151*(4), 413–433. https://doi.org/10.1007/s00410-006-0068-5
73. Whitehouse, M. J., & Platt, J. P. (2003). Dating high-grade metamorphism - Constraints from rare-earth elements in zircon and garnet. *Contributions to Mineralogy and Petrology*, *145*(1), 61–74. https://doi.org/10.1007/s00410-002-0432-z
74. Wipperfurth, S. A., Guo, M., Šrámek, O., & McDonough, W. F. (2018). Earth's chondritic Th/U: Negligible fractionation during accretion, core formation, and crust–mantle differentiation. *Earth and Planetary Science Letters*, *498*, 196–202. https://doi.org/10.1016/j.epsl.2018.06.029
75. Wotzlaw, J. F., Bindeman, I. N., Stern, R. A., D'Abzac, F. X., & Schaltegger, U. (2015). Rapid heterogeneous assembly of multiple magma reservoirs prior to Yellowstone supereruptions. *Scientific Reports*, *5*, 14026. https://doi.org/10.1038/srep14026
76. Xiang, W., Griffin, W. L., Chen, J., Huang, P., & Li, X. (2011). U and Th Contents and Th/U Ratios of Zircon in Felsic and Mafic Magmatic Rocks: Improved Zircon-Melt Distribution Coefficients. *Acta Geologica Sinica*, *85*(1), 164–174. https://doi.org/10.1111/j.1755-6724.2011.00387.x
77. Yakymchuk, C., Kirkland, C. L., & Clark, C. (2018). Th/U ratios in metamorphic zircon. *Journal of Metamorphic Geology*, *36*(6), 715–737. https://doi.org/10.1111/jmg.12307
78. Yang, X., Gaillard, F., & Scaillet, B. (2014). A relatively reduced Hadean continental crust and implications for the early atmosphere and crustal rheology. *Earth and Planetary Science Letters*, *393*, 210–219. https://doi.org/10.1016/J.EPSL.2014.02.056
79. Zhong, S., Feng, C., Seltmann, R., Li, D., & Dai, Z. (2018a). Geochemical contrasts between Late Triassic ore-bearing and barren intrusions in the Weibao Cu–Pb–Zn deposit, East Kunlun Mountains, NW China: constraints from accessory minerals (zircon and apatite). *Mineralium Deposita*, *53*(6), 855–870. https://doi.org/10.1007/s00126-017-0787-8

80. Zhong, S., Feng, C., Seltmann, R., Li, D., & Qu, H. (2018b). Can magmatic zircon be distinguished from hydrothermal zircon by trace element composition? The effect of mineral inclusions on zircon trace element composition. *Lithos*, *314–315*, 646–657. https://doi.org/10.1016/j.lithos.2018.06.029
81. Zou, X., Qin, K., Han, X., Li, G., Evans, N. J., Li, Z., & Yang, W. (2019). Insight into zircon REE oxy-barometers: A lattice strain model perspective. *Earth and Planetary Science Letters*, *506*, 87–96. https://doi.org/10.1016/J.EPSL.2018.10.031

References for compiled zircon dataset

1. Akinin, V. V., Andronikov, A. V., Mukasa, S. B., & Miller, E. L. (2013). Cretaceous lower crust of the continental margins of the northern pacific: Petrological and geochronological data on lower to middle crustal xenoliths. *Petrology*, *21*(1), 28–65. https://doi.org/10.1134/S0869591113010013
2. Anderson, A., Wirth, R., & Thomas, R. (2008). The alteration of metamict zircon and its role in the remobilization of high-field-strength elements in the Georgeville granite, Nova Scotia. *Canadian Mineralogist*, *46*(1), 1–18. https://doi.org/10.3749/canmin.46.1.1
3. Cai, K., Sun, M., Xiao, W., Yuan, C., Zhao, G., Long, X., Tumurkhuu, D., Zhou, K. (2014). Petrogenesis of late Paleozoic tholeiitic, Nb-enriched, calc-alkaline and adakitic rocks in southwestern Mongolia: Implications for intra-oceanic arc evolution. *Lithos*, *202–203*, 413–428. https://doi.org/10.1016/j.lithos.2014.06.004
4. Colón, D. P., Bindeman, I. N., Ellis, B. S., Schmitt, A. K., & Fisher, C. M. (2015). Hydrothermal alteration and melting of the crust during the Columbia River Basalt-Snake River Plain transition and the origin of low-δ18O rhyolites of the central Snake River Plain. *Lithos*, *224–225*, 310–323. https://doi.org/10.1016/j.lithos.2015.02.022
5. Doroshkevich, A. G., Prokopyev, I. R., Izokh, A. E., Klemd, R., Ponomarchuk, A. V., Nikolaeva, I. V., & Vladykin, N. V. (2018). Isotopic and trace element geochemistry of the Seligdar magnesiocarbonatites (South Yakutia, Russia): Insights regarding the mantle evolution beneath the Aldan-Stanovoy shield. *Journal of Asian Earth Sciences*, *154*, 354–368. https://doi.org/10.1016/j.jseaes.2017.12.030
6. Dou, J., Siebel, W., He, J., & Chen, F. (2019). Different melting conditions and petrogenesis of peraluminous granites in western Qinling, China, and tectonic implications. *Lithos*, *336–337*, 97–111. https://doi.org/10.1016/j.lithos.2019.04.003
7. El-Bialy, M. Z., & Ali, K. A. (2013). Zircon trace element geochemical constraints on the evolution of the Ediacaran (600-614Ma) post-collisional Dokhan Volcanics and Younger Granites of SE Sinai, NE Arabian-Nubian Shield. *Chemical Geology*, *360–361*, 54–73. https://doi.org/10.1016/j.chemgeo.2013.10.009
8. Janoušek, V., Holub, F. V., Verner, K., Čopjaková, R., Gerdes, A., Hora, J. M., Košler, J., Tyrrell, S. (2019). Two-pyroxene syenitoids from the Moldanubian Zone of the Bohemian Massif: Peculiar magmas derived from a strongly enriched lithospheric mantle source. *Lithos*, *342–343*, 239–262. https://doi.org/10.1016/j.lithos.2019.05.028
9. Kay, S. M., Jicha, B. R., Citron, G. L., Kay, R. W., Tibbetts, A. K., & Rivera, T. A. (2019). The Calc-Alkaline Hidden Bay and Kagalaska Plutons and the Construction of the Central Aleutian

Oceanic Arc Crust. *Journal of Petrology*, *60*(2), 393–439. https://doi.org/10.1093/petrology/egy119

10. Kostrovitsky, S. I., Skuzovatov, S. Y., Yakovlev, D. A., Sun, J., Nasdala, L., & Wu, F. Y. (2016). Age of the Siberian craton crust beneath the northern kimberlite fields: Insights to the craton evolution. *Gondwana Research*, *39*, 365–385. https://doi.org/10.1016/j.gr.2016.01.008
11. Li, H., Wu, J. H., Evans, N. J., Jiang, W. C., & Zhou, Z. K. (2018). Zircon geochronology and geochemistry of the Xianghualing A-type granitic rocks: Insights into multi-stage Sn-polymetallic mineralization in South China. *Lithos*, *312–313*, 1–20. https://doi.org/10.1016/j.lithos.2018.05.001
12. Liu, L., Hu, R. Z., Zhong, H., Tang, Y. W., Yang, J. H., Li, Z., Zhao, J. L., Shen, N. P. (2018). New constraints on the Cretaceous geodynamics of paleo-Pacific plate subduction: Insights from the Xiaojiang–Beizhang granitoids, Zhejiang Province, southeast China. *Lithos*, *314–315*, 382–399. https://doi.org/10.1016/j.lithos.2018.06.020
13. Lu, L., Qin, Y., Li, Z. F., Yan, L. L., Jin, X., & Zhang, K. J. (2019). Diachronous closure of the Shuanghu Paleo-Tethys Ocean: Constraints from the Late Triassic Tanggula arc-related volcanism in the East Qiangtang subterrane, Central Tibet. *Lithos*, *328–329*, 182–199. https://doi.org/10.1016/j.lithos.2019.01.034
14. Lukács, R., Harangi, S., Bachmann, O., Guillong, M., Danišík, M., Buret, Y., Quadt, A., Dunkl, I., Fodor, L., Sliwinski, J., Soo, I., Szepesi, J. (2015). Zircon geochronology and geochemistry to constrain the youngest eruption events and magma evolution of the Mid-Miocene ignimbrite flare-up in the Pannonian Basin, eastern central Europe. *Contributions to Mineralogy and Petrology*, *170*(5–6), 1–26. https://doi.org/10.1007/s00410-015-1206-8
15. Paulsen, T., Deering, C., Sliwinski, J., Bachmann, O., & Guillong, M. (2017). New detrital zircon age and trace element evidence for 1450 Ma igneous zircon sources in East Antarctica. *Precambrian Research*, *300*, 53–58. https://doi.org/10.1016/j.precamres.2017.07.011
16. Poletti, J. E., Cottle, J. M., Hagen-Peter, G. A., & Lackey, J. S. (2016). Petrochronological constraints on the origin of the Mountain Pass ultrapotassic and carbonatite intrusive suite, California. *Journal of Petrology*, *57*(8), 1555–1598. https://doi.org/10.1093/petrology/egw050
17. Rivera, T. A., Schmitz, M. D., Jicha, B. R., & Crowley, J. L. (2016). Zircon petrochronology and 40Ar/39Ar sanidine dates for the mesa falls tuff: Crystal-scale records of magmatic evolution and the short lifespan of a large yellowstone magma chamber. *Journal of Petrology*, *57*(9), 1677–1704. https://doi.org/10.1093/petrology/egw053
18. Robinson, F. A., Foden, J. D., & Collins, A. S. (2015). Zircon geochemical and geochronological constraints on contaminated and enriched mantle sources beneath the Arabian shield, Saudi Arabia. *Journal of Geology*, *123*(5), 463–489. https://doi.org/10.1086/683192
19. Sawaki, Y., Suzuki, K., Asanuma, H., Okabayashi, S., Hattori, K., Saito, T., & Hirata, T. (2017). Geochemical characteristics of zircons in the Ashizuri A-type granitoids: An additional granite topology tool for detrital zircon studies. *Island Arc*, *26*(6), e12216. https://doi.org/10.1111/iar.12216
20. Slezak, P., & Spandler, C. (2019). Carbonatites as recorders of mantle-derived magmatism and subsequent tectonic events: An example of the Gifford Creek Carbonatite Complex, Western Australia. *Lithos*, *328–329*, 212–227. https://doi.org/10.1016/j.lithos.2019.01.028
21. Sun, J., Tappe, S., Kostrovitsky, S. I., Liu, C. Z., Skuzovatov, S. Y., & Wu, F. Y. (2018). Mantle sources of kimberlites through time: A U-Pb and Lu-Hf isotope study of zircon megacrysts from

the Siberian diamond fields. *Chemical Geology*, *479*, 228–240. https://doi.org/10.1016/j.chemgeo.2018.01.013

22. Tichomirowa, M., Whitehouse, M. J., Gerdes, A., Götze, J., Schulz, B., & Belyatsky, B. V. (2013). Different zircon recrystallization types in carbonatites caused by magma mixing: Evidence from U-Pb dating, trace element and isotope composition (Hf and O) of zircons from two Precambrian carbonatites from Fennoscandia. *Chemical Geology*, *353*, 173–198. https://doi.org/10.1016/j.chemgeo.2012.11.004
23. Verbaas, J., Thorkelson, D. J., Milidragovic, D., Crowley, J. L., Foster, D., Daniel Gibson, H., & Marshall, D. D. (2018). Rifting of western Laurentia at 1.38 Ga: The Hart River sills of Yukon, Canada. *Lithos*, *316–317*, 243–260. https://doi.org/10.1016/j.lithos.2018.06.018
24. Vilalva, F. C. J., Simonetti, A., & Vlach, S. R. F. (2019). Insights on the origin of the Graciosa A-type granites and syenites (Southern Brazil) from zircon U-Pb geochronology, chemistry, and Hf and O isotope compositions. *Lithos*, *340–341*, 20–33. https://doi.org/10.1016/j.lithos.2019.05.001
25. Wang, Q., Chung, S. L., Li, X. H., Wyman, D., Li, Z. X., Sun, W. D., Qiu, H.N., Liu, Y. S., Zhu, Y. T. (2012). Crustal melting and flow beneath northern Tibet: Evidence from mid-miocene to quaternary strongly peraluminous rhyolites in the Southern Kunlun Range. *Journal of Petrology*, *53*(12), 2523–2566. https://doi.org/10.1093/petrology/egs058
26. Yang, W. Bin, Niu, H. C., Shan, Q., Sun, W. D., Zhang, H., Li, N. B., Jiang, Y. H., Yu, X. Y. (2014). Geochemistry of magmatic and hydrothermal zircon from the highly evolved Baerzhe alkaline granite: implications for Zr–REE–Nb mineralization. *Mineralium Deposita*, *49*(4), 451–470. https://doi.org/10.1007/s00126-013-0504-1
27. Zhang, S. H., Zhao, Y., Yang, Z. Y., He, Z. F., & Wu, H. (2009). The 1.35 Ga diabase sills from the northern North China Craton: Implications for breakup of the Columbia (Nuna) supercontinent. *Earth and Planetary Science Letters*, *288*(3–4), 588–600. https://doi.org/10.1016/j.epsl.2009.10.023
28. Zhao, L., Guo, F., Fan, W., Zhang, Q., Wu, Y., Li, J., & Yan, W. (2016). Early Cretaceous potassic volcanic rocks in the Jiangnan Orogenic Belt, East China: Crustal melting in response to subduction of the Pacific-Izanagi ridge? *Chemical Geology*, *437*, 30–43. https://doi.org/10.1016/j.chemgeo.2016.05.011
29. Zheng, J., Griffin, L., O'Reilly, S. Y., Lu, F., Yu, C., Zhang, M., & Li, H. (2004). U-Pb and Hf-isotope analysis of zircons in mafic from Fuxian kimberlites: Evolution of the lower crust beneath the North China craton. *Contributions to Mineralogy and Petrology*, *148*(1), 79–103. https://doi.org/10.1007/s00410-004-0587-x
30. Zhu, M., Zhang, L., Dai, Y., Wang, C., & Peng, Z. (2017). Hydrothermal modification of zircon geochemistry and Lu–Hf isotopes from the Hongtoushan Cu–Zn deposit, China. *Ore Geology Reviews*, *86*, 707–718. https://doi.org/10.1016/j.oregeorev.2017.03.028

Acknowledgments

This study was financially supported by the NASA grant (80NSSC18K1612). Special thanks are given to my parents, professors, and groupmates for their guidance and unconditional supports on this study. Thank you, Dr. Dustin Trail for his kind encouragements. The compiled dataset

was acquired from 30 previously published works, which are listed in the supporting information file (supplementary file 1). The self-collected Greenland dataset was submitted to Earthchem (under review) and also accessible in the supporting information (supplementary file 2).